

Form Approved  
OMB No. 0704-0188

## REPORT DOCUMENTATION PAGE

Public reporting burden for this collection of information is estimated to average 1 hour per response, including the time for reviewing instructions, searching existing data sources, gathering and maintaining the data needed, and completing and reviewing the collection of information. Send comments regarding this burden estimate or any other aspect of this collection of information, including suggestions for reducing this burden, to Washington Headquarters Services, Directorate for Information Operations and Reports, 1215 Jefferson Davis Highway, Suite 1204, Arlington, VA 22202-4302, and to the Office of Management and Budget, Paperwork Reduction Project (0704-0188), Washington, DC 20503.

1. AGENCY USE ONLY (Leave blank)			2. REPORT DATE	3. REPORT TYPE AND DATES COVERED
			AUGUST 1994	Final Rept.: Jan 1/91--Jun 30/94
4. TITLE AND SUBTITLE			Unsteadiness of Shock-Induced Turbulent Boundary Layer Separation--- An Inherent Feature of Turbulent Flow or Solely a Wind Tunnel Phenomenon	
6. AUTHOR(S)			D. S. Dolling & M. E. Erengil	
7. PERFORMING ORGANIZATION NAME(S) AND ADDRESS(ES)			Center for Aeromechanics Research, WRW 220 The University of Texas at Austin Austin, TX 787121085	
9. SPONSORING/MONITORING AGENCY NAME(S) AND ADDRESS			U. S. Army Research Office P. O. Box 12211 Research Triangle Park, NC 27709-2211	
11. SUPPLEMENTARY NOTES			The view, opinions and/or findings contained in this report are those of the author(s) and should not be construed as an official Department of the Army position, policy, or decision, unless so designated by other documentation.	
12a. DISTRIBUTION/AVAILABILITY STATEMENT			Approved for public release; distribution unlimited.	
13. ABSTRACT			<p>The purpose of this work was to (i) examine separation shock wave unsteadiness in different turbulent interactions and determine whether a universal model describing the unsteadiness could be developed, and (ii) determine whether or not the observed unsteadiness is a feature of turbulent flow in general, or is specific to the wind tunnel environment. To this end, wall and pitot pressure fluctuation measurements were made in interactions generated by unswept and 25 deg swept compression ramp models, and by 8 deg and 30 deg swept blunt-fin models in a high Reynolds number, Mach 5 turbulent boundary layer.</p> <p>It is clear that the high-frequency, jittery motion of the separation shock is the result of the passage through the wave of individual large-scale turbulent structures. Thus, this component of the unsteadiness is an inherent feature of all turbulent flows. The primary outstanding question concerns the cause of the low-frequency expansion/contraction of the separated flow which is characterized by the large-scale, long-duration excursions of the separation shock wave.</p> <p>Preliminary experimental work to address this question has revealed two very interesting, complementary results. First, there is a distinct correlation between large-scale expansion or contraction of the separated flow and long duration (i.e., low-frequency) falls or rises in pitot pressure in the incoming turbulent boundary layer. Second, results from the same experiment show that the ensemble-averaged pitot pressure at a fixed location in the incoming undisturbed boundary layer correlates with separation shock wave position.</p> <p>These results suggest a model in which the boundary layer "thickens and thins" as it flows downstream. However, at this stage it must be emphasized that the "thickening-thinning" boundary-layer model is an inference and that there is no direct time-resolved evidence. In this context it should be noted that some evidence has been found of Taylor-Gortler vortices in the incoming flow, and it is possible that these play a role in the physics. Confirmation is extremely difficult using intrusive instrumentation alone, and, in the next phase of the work, both conventional instrumentation and planar laser imaging techniques will be used to explore the incoming flow structure corresponding to different separated bubble states and dynamics.</p>	
14. SUBJECT TERMS			15. NUMBER OF PAGES	
Unsteady turbulent boundary layer separation, shock wave-induced separation			53	
17. SECURITY CLASSIFICATION OF REPORT			16. PRICE CODE	
UNCLASSIFIED			17. SECURITY CLASSIFICATION OF THIS PAGE	
UNCLASSIFIED			19. SECURITY CLASSIFICATION OF ABSTRACT	
UNCLASSIFIED			20. LIMITATION OF ABSTRACT	
			UL	
NSN 7540-01-280-5500				

**Unsteadiness of Shock-Induced  
Turbulent Boundary Layer Separation—  
An Inherent Feature of Turbulent Flow or  
Solely a Wind Tunnel Phenomenon**

**Final Report**

*by*

**D. S. Dolling & M. E. Erengil**  
**Center for Aeromechanics Research**

Accesion For	
NTIS	CRA&I <input checked="" type="checkbox"/>
DTIC	TAB <input type="checkbox"/>
Unannounced	<input type="checkbox"/>
Justification .....	
By _____	
Distribution /	
Availability Codes	
Dist	Avail and / or Special
A-1	

**August 1994**

**Grant No. DAAL03-91-G-0023**

**The University of Texas at Austin**

**Approved for Public Release  
Distribution Unlimited**

## Table of Contents

<b>Foreword.....</b>	i
<b>Nomenclature.....</b>	iii
<b>1. Introduction.....</b>	1
<b>2. Experimental Program .....</b>	3
<i>2.1. Wind tunnel and flow conditions.....</i>	3
<i>2.2. Models and transducer plug.....</i>	4
<i>2.3. Instrumentation and data acquisition system .....</i>	5
<i>2.4. Test program.....</i>	6
<b>3. Analysis Techniques .....</b>	6
<i>3.1. Box-car conversion technique .....</i>	6
<i>3.2. Derivation of separation shock position and velocity histories.....</i>	7
<i>3.3. Derivation of instantaneous pressure ratio history.....</i>	8
<i>3.4. Variable interval cross-correlation .....</i>	8
<i>3.5. Digital filter .....</i>	8
<i>3.6. CFD model.....</i>	9
<b>4. Discussion of Results .....</b>	9
<i>4.1. Mean, standard deviation, and intermittency distributions.....</i>	9
<i>4.2. Power spectral densities of <math>X_s(t)</math> and <math>V_s(t)</math> .....</i>	10
<i>4.3. Correlation of <math>V_s(t)</math> with pressure ratio fluctuations.....</i>	11
<i>4.4. Correlation of <math>V_s(t)</math> with upstream pressure fluctuations .....</i>	11
<i>4.5. Correlation of <math>V_s(t)</math> with downstream pressure fluctuations.....</i>	13
<i>4.6. Correlation of <math>X_s(t)</math> with downstream pressure fluctuations.....</i>	14
<i>4.7. Physical model of the unsteadiness .....</i>	15
<i>4.8. Source of low-frequency component.....</i>	16
<i>4.9. Results from computational analysis.....</i>	19
<b>5. Conclusions.....</b>	20
<b>6. Listing of Participating Scientific Personnel &amp; Advanced Degrees Awarded.....</b>	22
<b>7. Listing of All Publications &amp; Technical Reports.....</b>	23
<b>REFERENCES.....</b>	24
<b>FIGURES.....</b>	26

## Foreword

The purpose of this work was to (i) examine separation shock wave unsteadiness in different turbulent interactions and determine whether a universal model describing the unsteadiness could be developed, and (ii) determine whether or not the observed unsteadiness is a feature of turbulent flow in general, or is specific to the wind tunnel environment. To this end, wall and pitot pressure fluctuation measurements were made in interactions generated by unswept and 25 deg swept compression ramp models, and by 8 deg and 30 deg swept blunt-fin models in a high Reynolds number, Mach 5 turbulent boundary layer. Using a new conditional sampling algorithm, the separation shock unsteadiness was characterized in terms of its position and velocity histories. These fluctuations were then correlated with conditionally extracted static pressure ratio across the separation shock, and with wall pressure measurements made upstream and downstream of the region of shock unsteadiness. Results show that separation shock unsteadiness can be caused by two different physical phenomena. The small-scale or jittery motion is caused by perturbations in the ratio of static quantities across the shock foot. These perturbations induce fluctuations in the separation shock velocity and thus changes in separation shock position are an integral result of the velocity fluctuations. The large-scale or global motion of the separation shock is caused by the expansion and contraction or trembling motion of the separation bubble. An expansion of the separation bubble, for example, displaces the separation shock to an upstream position, whereas a contraction of the bubble results in a displacement in the downstream direction. In addition to experimental results, computations of an inviscid, unsteady, quasi one-dimensional flow have also been performed. Although this does not model the experimental conditions, the analysis provides computational support for the explanation offered for the small-scale jittery motion of the separation shock.

As described above, it is clear that the high-frequency, jittery motion of the separation shock is the result of the passage through the wave of individual large-scale turbulent structures. Thus, it is reasonable to conclude that this component of the unsteadiness is an inherent feature of all turbulent flows. The primary outstanding question concerns the cause of the low-frequency expansion/contraction of the separated flow which is characterized by the large-scale, long-duration excursions of the separation shock wave.

Preliminary experimental work to address this question has revealed two very interesting, complementary results. First, there is a distinct correlation between large-scale expansion or contraction of the separated flow and long duration (i.e., low-frequency) falls or rises in pitot pressure in the incoming turbulent boundary layer. The time scale of these gradual rises and falls in pitot pressure is around 1 ms, almost two orders of magnitude higher than the large eddy time scale  $\delta_1/U_\infty$ . Thus, these rises and falls in pitot pressure are not generated by individual turbulent structures, but are caused by low-frequency "global" motion of the boundary layer. Second, results from the same experiment show that the ensemble-averaged pitot pressure at a fixed location in the incoming undisturbed boundary layer correlates with separation shock wave position.

These two sets of results suggest a model in which the boundary layer "thickens and thins" as it flows downstream. In such a simple model, a higher pitot pressure at a fixed height would imply a fuller velocity profile than the mean profile, one more resistant to separation,

which would generate a smaller separation bubble than would the mean profile. Conversely, a lower pitot pressure at a fixed height would imply a slightly retarded profile which would generate a larger separation bubble than would the mean profile. However, at this stage it must be emphasized that the "thickening-thinning" boundary-layer model is an inference and that there is no direct time-resolved evidence. In this context it should be noted that some evidence has been found of Taylor-Gortler vortices in the incoming flow, and it is possible that these play a role in the physics. Confirmation is extremely difficult using intrusive instrumentation alone, and, in the next phase of the work, both conventional instrumentation and planar laser imaging techniques will be used to explore the incoming flow structure corresponding to different separated bubble states and dynamics.

## Nomenclature

$C_f$	skin friction coefficient
$D$	cylinder or blunt-fin leading edge diameter
$G$	power spectral density coefficient
$H$	shape factor
$M$	Mach number
$P$	pressure
$R$	cross-correlation coefficient
$R_c$	computed pressure ratio across normal shock
$R_s$	measured pressure ratio across separation shock
$Re$	unit Reynolds number
$T$	threshold
$U$	velocity
$V_c$	computed normal shock velocity
$V_s$	measured separation shock velocity
$X_c$	computed normal shock position
$X_s$	measured separation shock position
$f$	fall-time or frequency
$h$	channel height
$p$	pressure
$r$	rise-time
$t$	time
$x$	streamwise distance
$z$	spanwise distance
$\Delta Y$	ordinate offset
$\Pi$	boundary layer wake strength parameter
$\delta_0$	boundary layer thickness
$\delta^*$	boundary layer displacement thickness
$\lambda$	sweepback angle
$\gamma$	separation shock intermittency factor
$\theta$	boundary layer momentum deficit thickness
$\rho$	density

$\sigma$	standard deviation
$\tau$	time-delay
$\zeta$	transducer spacing
$(\bar{})$	mean value

*Subscripts*

EA	ensemble-averaged
d	downstream
i	channel inlet
o	channel outlet or incoming conditions
t	stagnation quantities
u	upstream
w	wall conditions
$\infty$	freestream conditions

*Abbreviations*

Ch	channel
FIR	Finite Impulse Response
LDV	Laser Doppler Velocimeter
S	separation
SBF-30	30 deg swept blunt-fin
SBF-8	8 deg swept blunt-fin
SCR-25	25 deg swept compression ramp
UCR	unswept compression ramp
UI	upstream influence
VITA	Variable Interval Time Averaging

## 1. Introduction

Shock wave/turbulent boundary layer interactions are important in a wide variety of internal and external aerothermodynamics problems of interest to the U.S. Army. They include flows over transonic rotor blades, around high speed missile control surfaces and fins, and upstream of a missile base where unsteady separation is induced by the plume. Plume-induced separation effects can play a critical role in determining missile base drag and plume signature. Consequently, there has been a very large number of studies of these interactions over the past four decades. Although high speed cinematography from the 1950's (Bogdonoff 1955, Chapman *et al.* 1958) showed that the shock-induced turbulent separation was unsteady, the lack of adequate instrumentation resulted in most studies being of mean flow properties only. Kistler (1964) was probably the first to make detailed wall pressure measurements under separated supersonic turbulent boundary layer, and the first to discuss the intermittent character of the wall pressure signal caused by the translating separation shock wave. Since Kistler there has been an increasing number of studies focusing on interaction unsteadiness. The qualitative character and quantitative details of the unsteadiness naturally vary from one flow type to another, but typically the unsteadiness manifests itself as a large-scale, low-frequency pulsation of the separated flow and flapping of the outgoing boundary layer. A recent review of much of this work has been compiled by Dolling (1993).

From an engineering perspective the unsteadiness is important from two points of view. First, it results in large amplitude fluctuating loads (as high as 185 dB) which can substantially shorten the fatigue life of vehicle components. Second, it compounds the difficulties of drawing conclusions from comparisons of experimental data with computations. The former are largely time-averaged data from an unsteady flowfield whereas the latter represent converged or steady state flowfields. The difficulties of drawing meaningful conclusions from such comparisons are discussed by Dolling (1992) and Marshall & Dolling (1992). Clearly, an understanding of the physical causes of the unsteadiness is needed, not only to understand the flowfield physics but to assist in the development of appropriate modeling strategies. At the present time, understanding of the physical mechanisms is incomplete, although as outlined below there has been progress over the past few years.

Andreopoulos & Muck (1987) made wall pressure measurements in Mach 3 compression ramp interactions, and reported that the mean separation shock wave period was independent of position in the intermittent region and independent of the ramp angle. The intermittent region is the region within which the separation shock translates. The zero-crossing frequency, which is simply the number of unidirectional shock crossings over a given transducer in the intermittent region, was found to be  $0.13 U_\infty / \delta_0$ , where  $U_\infty$  is the freestream velocity and  $\delta_0$  is the incoming boundary layer thickness. Since this frequency was the same order as the estimated bursting frequency in the incoming turbulent boundary layer and since the measured shock speeds were the same order as velocity fluctuations in the flowfield, Andreopoulos & Muck argued that "the incoming boundary layer is largely responsible for the shock motion." If the shock frequency is controlled by turbulent bursts and/or velocity fluctuations, then this reasoning would suggest that in a given incoming boundary layer the shock zero-crossing frequency and the streamwise extent of its motion would be fixed. This certainly is not the case. For cylinder-induced interactions in a fixed incoming boundary layer, the zero-crossing frequency decreases and the streamwise extent of the shock motion increases as the cylinder diameter  $D$  increases (Dolling & Smith 1989). In fact, the intermittent region length is essentially  $0.8 D$ , independent of boundary layer thickness. Furthermore, since the one-threshold technique used by Andreopoulos & Muck has been shown to overestimate shock frequencies significantly because of its inability to discriminate between shock-induced and turbulent pressure fluctuations (Dolling & Brusniak 1989), it is probable that changes in shock frequency with ramp angle were not detected.

In a later study, Tran (1986) made simultaneous wall pressure measurements under the incoming boundary layer and near the upstream influence line in the interaction generated by a 20 deg compression ramp model. The experiments were made in the same test facility used by Andreopoulos & Muck (1987). Using the Variable Interval Time Averaging (VITA) technique, Tran found little correlation between "events" detected on the upstream channel and the shock-induced pressure pulses on the downstream channel. He concluded that the pressure pulses in the intermittent region were independent of the large-scale turbulent structures in the upstream boundary layer which are convected into the interaction. Tran's conclusions, however, must also be treated with some caution. He used only a single transducer in the intermittent region, close to its upstream edge. It is probable that the separation shock moved upstream and downstream in response to the turbulent structures, but remained downstream of the measuring transducer. With hindsight, it would be better to use the shock-induced pressure pulse on downstream transducer as the trigger and ensemble average on the upstream channel in the undisturbed boundary layer.

This approach was adopted by Erengil & Dolling (1991b) and later refined by McClure (1992). Simultaneous measurements were made of wall pressure fluctuations under the incoming boundary layer and the intermittent region of a Mach 5 compression ramp interaction. Conditional sampling algorithms and a variable window ensemble averaging technique were used to investigate the correlation between specific separation shock motions and pressure fluctuations in the incoming turbulent boundary layer. Although the correlation was clearly evident for turn-around motions of the separation shock, the interpretation of the results corresponding to upstream and downstream sweeps was not clear due to an insufficient number of ensembles. Nevertheless, to the best of the authors' knowledge, these results were probably the first to show a direct correlation between pressure fluctuations in the incoming boundary layer and the separation shock motion.

The interpretation of the results corresponding to upstream and downstream motions of the separation shock has since been clarified by McClure (1992). The experimental arrangement was the same as that of Erengil & Dolling (1991b). McClure combined sweep motions from different positions in the intermittent region, creating a large number of ensembles for a given sweep motion, say an upstream sweep over three transducers. These results showed that the correlation seen in the turn-around motions was not unique to these motions, and that similar correlations also exist for upstream and downstream sweep motions of the shock. Most importantly, the characteristic shapes of the ensemble signatures on the upstream channels are different for the different shock motions. Specifically, the pressure signatures for the upstream sweeps have a rise-fall-rise sequence, whereas those for the downstream sweeps have a fall-rise-fall sequence. Also, analysis of the timing of events showed that these signatures are convected into the interaction and are coincident with the separation shock foot at the time of the crossing over a given transducer. The structures causing these signatures convect downstream pass through the shock and continue downstream through the interaction at convection speeds of about  $0.75 U_\infty$ . Their temporal extent is about 75 to 100  $\mu s$ , which corresponds to a spatial extent of about  $3.2$  to  $4.3 \delta_0$ . In an extension of McClure's work, Gramann & Dolling (1992) detected the signatures as far upstream as  $20 \delta_0$  from the interaction.

Gramann (1989) studied the dynamics of the separation bubble in a Mach 5 compression ramp interaction. Using conditional sampling algorithms as well as standard analysis techniques applied to wall pressure fluctuation measurements, he specifically examined the relative motion of the separation and reattachment lines in this interaction. His results showed that the separation bubble undergoes an expansion and contraction type motion in which the separation and reattachment lines move away from and towards each other. Similar observations were also made earlier by Kussoy *et al.* (1987) in a Mach 3 cylinder-flare interaction. In the latter study, high speed shadow movies and LDV measurements were made simultaneously

with wall pressure measurements under the unsteady separation shock. Results on the plane of symmetry showed that the separation bubble "expanded and contracted like a balloon."

In another study, Selig & Smits (1991) applied periodic blowing to the boundary layer at various locations within the separated region generated by a 24 deg compression ramp in a Mach 3 flow. Blowing was applied through a slot across the full span at a rate of either 2.5 or 9 percent of the freestream mass flux at frequencies up to 5 kHz. Wall pressure and mass flux fluctuation measurements were made and stroboscopic schlieren videography was used to observe the unsteady flowfield. As the slot was moved closer to the separation shock foot, the shock motion could be locked in to the blowing frequency and completely controlled by the periodic blowing. Although the upstream influence had increased, the rms levels in the vicinity of the separation shock did not change appreciably. Based on cross-correlation results and their success in the control of the unsteadiness, Selig and Smits concluded that "it seems probable that the unsteadiness of the shock for the 24 deg compression corner is partially driven by large-scale fluctuations in the separated region."

Although some of these earlier studies show a direct correlation between separation shock motion and pressure fluctuations in the incoming turbulent boundary layer, they fail to provide a physical model by which these turbulent structures are related to the separation shock unsteadiness. By the same token, although those studies investigating a possible correlation between separation shock motion and dynamics of the separation bubble have demonstrated the characteristic motion of the latter, they too have not been successful in providing a physical model which explains the unsteadiness. This is a particularly difficult task since separation shock motion and dynamics of the separation bubble as well as fluctuations in the separated flow are highly coupled.

The purpose of the study reported in this paper, is to examine separation shock unsteadiness in different interactions and first determine whether a universal model describing and explaining the unsteadiness could be developed. The second objective was to try and determine if the results are an inherent feature of all turbulent flows or whether they are a feature seen solely in wind-tunnel-generated boundary layers. To do this, existing measurements from different interactions have been used and also new experiments performed whenever necessary. Measurements from unswept and 25 deg swept compression ramp flows, and from 8 deg and 30 deg swept blunt-fin interactions have been analyzed. Using simultaneously sampled multi-channel wall pressure fluctuations, separation shock foot position history,  $X_s(t)$  and velocity history,  $V_s(t)$  have been determined. Once they were determined, these histories were correlated with conditionally extracted static pressure ratio,  $R_s(t)$ , across the separation shock, and with wall pressure measurements made upstream and downstream of the intermittent region. In this paper, the discussion of these and other results are followed by the description of a physical model describing the separation shock unsteadiness in shock wave / turbulent boundary layer interactions.

In addition to the experimental results, computations of an unsteady, inviscid and quasi one-dimensional flow are also presented. It should be emphasized that the purpose of this work is not to model the unsteadiness in these interactions. Instead, the CFD calculations were used as a tool to further demonstrate *one* part of the physical mechanism of unsteadiness obtained from experimental results.

## 2. Experimental Program

### 2.1. Wind tunnel and flow conditions

The experiments were conducted in the high Reynolds number, Mach 5 blowdown wind tunnel at Balcones Research Center of the University of Texas at Austin. The tunnel has

a rectangular test section which is 15.24 cm (6 in.) wide, 17.78 cm (7 in.) high, and 30.48 cm (12 in.) long. Up to  $3.964 \text{ m}^3$  (140 ft<sup>3</sup>) of compressed air stored at about 17.24 MPa (2500 psia) provides run times of up to 1 min. for the current stagnation conditions. The incoming air is heated by two 420 kW banks of nichrome wire resistive heaters located upstream of the stagnation chamber. These heaters can provide stagnation temperatures of up to 422 K (759 °R).

All tests were conducted at a stagnation pressure of 2.28 MPa (330 psia) and a stagnation temperature of 359 K (647 °R), which generate a freestream unit Reynolds number of  $49.9 \times 10^6 \text{ m}^{-1}$  ( $15.2 \times 10^6 \text{ ft}^{-1}$ ). The freestream Mach number and velocity in the test section were 4.95 and 775 m/s (2543 ft/s), respectively. The incoming turbulent boundary layer underwent natural transition and developed under approximately adiabatic wall temperature conditions. Boundary layer parameters were determined from pitot surveys made with a probe having a tip orifice 0.020 cm (0.008 in.) high and 0.038 cm (0.015 in.) wide. Total temperature surveys were also made using thermocouple probes. In the data reduction, the static pressure through the boundary layer was assumed constant and equal to the freestream value. A good fit to law-of-the-wall / law-of-the-wake was obtained for the mean velocity profile. Boundary layer parameters measured at 96.47 cm (37.98 in.) downstream of the throat on the tunnel centerline, approximately  $3 \delta_0$  upstream of the models, are listed in table 1 (McClure 1992).

---

$\delta_0$	=	1.51 cm	(0.59 in.)
$\delta^*$	=	0.67 cm	(0.26 in.)
$\theta$ ( $\times 10^2$ )	=	6.61 cm	(2.60 in.)
$\Pi$	=	0.78	
$H \equiv \delta^*/\theta$	=	10.20	
$Re_\theta$ ( $\times 10^{-4}$ )	=	3.16	
$C_f$ ( $\times 10^4$ )	=	7.74	

---

TABLE 1. Boundary layer parameters.

---

## 2.2. Models and transducer plug

Several models have been used to generate different interactions. These include unswept and 25 deg swept compression ramp models, and 8 deg and 30 deg swept blunt-fin models.

The unswept 28 deg compression ramp model was made of aluminum and was 12.07 cm (4.75 in.) wide and 3.8 cm (1.5 in.) high. Two aluminum aerodynamic fences with sharpened leading edges were attached to the sides of the ramp to prevent spillage and isolate the interaction from the sidewall boundary layers. The 25 deg swept compression ramp model was made of brass and was 10.8 cm (4.25 in.) wide and 5.1 cm (2 in.) high. It had a constant streamwise angle of 28 deg. For the swept ramp only one stainless steel fence was attached to the apex side of the model and the fence leading edge extended at least 6.4 cm (2.5 in.) up-

stream of the apex. Both blunt-fin models were made of aluminum. They had a leading edge diameter of 1.9 cm (0.75 in.) and were 10.16 cm (4 in.) high. All models were mounted on the tunnel floor and could be moved in the streamwise direction. Sketches of these models and their appropriate coordinate systems are shown in Fig. 1.

The brass instrumentation plug, which was 8.57 cm (3.375 in.) in diameter, was centered 97.00 cm (38.19 in.) downstream of the nozzle throat and installed in the test section floor. In this plug, the transducers could be mounted flush along four different rows which could be aligned at any angle to the freestream. The first row was along the plug centerline and it had 26 transducer ports. The second (8 ports), third (13 ports), and fourth (12 ports) were parallel to the center row and were spaced 0.29 cm (0.115 in.), 1.27 cm (0.5 in.), and 2.54 cm (1 in.) from the latter, respectively. In any given row, the center-to-center spacing between two adjacent ports,  $\zeta$ , was 0.29 cm (0.115 in.). Customized dummy brass plugs were mounted flush in the unused transducer ports.

### *2.3. Instrumentation and data acquisition system*

Up to eight miniature, Kulite, high-frequency response pressure transducers were used. These were either XCW-062-15A, 0-103 kPa (0-15 psia) or XCQ-062-50A, 0-345 kPa (0-50 psia) absolute pressure transducers. Transducers were installed either flush with the floor to measure fluctuating wall pressure or inside of small probes used to measure fluctuating pitot pressure. They all had outer diameters of 0.159 cm (0.0625 in.) and 0.071 cm (0.028 in.) diameter pressure sensitive diaphragms. As quoted by the manufacturer, the natural frequency response of the diaphragm was 250 kHz for 0-103 kPa models and 500 kHz for 0-345 kPa models. However, perforated screens protecting the transducers from dust particles limit the effective frequency response of both models to about 50 kHz. All transducers were calibrated statically using a Heise digital pressure gauge (Model 710A) accurate to within 6.9 Pa (0.001 psia).

Output from pressure transducers was first amplified by either Dynamics (Model 7525), Measurements Group (Model 2311), or PARC (Model 113) amplifiers, and then low-pass filtered using Ithaco (Model 4113 or Model 4213) analog filters. Amplifier gains were adjusted for maximum resolution and varied depending on the transducer model and its position in the interaction. Filter cut-off frequencies were set at 50 kHz unless the sampling frequency required a lower setting.

Filtered signals were then digitized by two LeCroy Model 6810 Waveform Recorders equipped with 12-bit analog-to-digital (A/D) converters. Each of these recorders had two Megawords of memory, and could sample 1 channel of data at rates up to 5 MHz per channel, or 4 channels of data simultaneously, at rates up to 1 MHz per channel. Both A/D converters were triggered using the same clock, thus either 2 channels could be sampled simultaneously at rates up to 5 MHz per channel, or 8 channels at rates up to 1 MHz per channel. A maximum of 4096 records (1 record = 1024 datapoints) of data could be obtained. Further, each channel could be adjusted independently allowing the user to optimize each channel for different input signal ranges.

Data were then downloaded to an HP 9000 Model 380 workstation and stored on magnetic tapes for later analysis. All subsequent analyses were performed either on the primary computer (Model 380) or on one of the two HP 9000 Model 340 workstations connected to the primary computer.

#### 2.4. Test program

The main purpose of this work was to examine the separation shock unsteadiness observed in different interactions, to determine whether a universal model describing the causes of unsteadiness could be developed, and to understand the source of the unsteadiness. To this end, the authors made use of existing measurements performed by themselves and their colleagues in the same facility. Experiments in the unswept and swept compression ramp interactions were performed by Erengil & Dolling (1993). Those in swept blunt-fin interactions were done by Kleifges & Dolling (1993). In addition to these, some new experiments have been performed by the authors in interactions generated by the unswept compression ramp and the 8 deg swept blunt-fin models. In all these experiments, at least six transducers were placed upstream of the separation line to measure the separation shock dynamics. The location of the separation line (i.e., line of coalescence of surface streaklines) is usually determined from surface tracer techniques. In this case, kerosene-diesel-lampblack mixture is painted on the tunnel floor prior to a flow visualization run, and the pattern is lifted off the surface on large sheets of transparent tape. The remaining transducers were used to measure wall pressure fluctuations under the incoming turbulent boundary layer and/or under the separated shear layer.

In all the interactions studied, the unsteadiness is characterized by the separation shock position,  $X_s(t)$ , and velocity,  $V_s(t)$ , histories which are derived from simultaneous measurements of wall pressure fluctuations in the intermittent region. Consequently, to determine  $X_s(t)$  and  $V_s(t)$  accurately, one must use as many transducers as possible within the intermittent region of a given interaction. This will be clearer as the derivation of these quantities is explained in the following section.

### 3. Analysis Techniques

Standard time-series analysis techniques as well as conditional sampling algorithms have been used to analyze the experimental data. In the conditional sampling techniques employed here the separation shock position,  $X_s(t)$ , and velocity,  $V_s(t)$ , histories are calculated. Before discussing the derivation of these quantities in some detail, it will be helpful to first describe the box-car conversion technique briefly since  $X_s(t)$  and  $V_s(t)$  are deduced from nested box-car sequences. A detailed description of the two-threshold box-car conversion technique has been published by Dolling & Brusniak (1989).

#### 3.1. Box-car conversion technique

The two-threshold box-car conversion technique is used to extract shock passages from wall pressure fluctuations measured under the unsteady separation shock. In this method, the thresholds are set at  $T_1 = \bar{P}_{wo} + 3\sigma_{Pwo}$  and  $T_2 = \bar{P}_{wo} + 6\sigma_{Pwo}$ , where  $\bar{P}_{wo}$  is the undisturbed turbulent boundary layer mean pressure level and  $\sigma_{Pwo}$  is the rms of the turbulent boundary layer pressure fluctuations. These threshold settings were recommended following a sensitivity analysis of the effects of varying  $T_1$  and  $T_2$  (Dolling & Brusniak 1989). A similar sensitivity analysis showed that the same threshold settings were appropriate for the analysis of data from swept flows (Erengil & Dolling 1993). In the two-threshold method, the box-car is generated when  $P_w(t) > T_2$  and is terminated when  $P_w(t) < T_1$ . Thus when the box-car assumes a value of 1, this indicates a shock passage in the upstream direction and is called the rise-time. Similarly, when it assumes a value of 0, this indicates a shock passage in the downstream direction and is called the fall-time. Once a shock passage is detected using  $T_1$  and  $T_2$  and an initial fall-time assigned, a counter is then used to march backward in time until the instantaneous value of  $P_w(t)$ , which is just below  $T_2$ , is found. The fall-time is then reassigned to this new value. The requirement that the rise- and fall-times be determined by the same threshold level (i.e.,  $T_2$ ) ensures that the separation shock foot is at the same position at

both rise- and fall-times. The relative position of the transducer and its rise- and fall-times are the only pertinent information for the derivation of the separation shock position history. Typical wall pressure signals from the unswept compression ramp interaction and corresponding box-car sequences are shown in Figs. 2a through 2f.

### 3.2. Derivation of separation shock position and velocity histories

Separation shock position history is deduced from nested box-car sequences which are generated from simultaneous measurements of multi-channel wall pressure fluctuations made in the intermittent region. The schematic at top of Fig. 2 shows the position of eight transducers, spaced  $1\zeta$  apart, upstream of the separation line in the interaction generated by the unswept compression corner. Given eight transducers, there are nine discrete bins in which the separation shock foot can be bracketed. In this case, a bin is defined as the spatial region from the downstream end of one transducer to the downstream end of the adjacent transducer as indicated in the schematic. Simultaneous wall pressure fluctuations and corresponding box-car sequences measured at stations indicated by filled markers are plotted in Figs. 2a through 2f for channels 1 through 6, respectively. As was discussed earlier, the rise- and fall-times of a given box-car sequence indicate shock passages in the upstream and downstream directions. Some of these times are indicated in Figs. 2c through 2e. The box-car sequences shown in Figs. 2a through 2f are plotted again in the nested form in Fig. 2g. The rise- and fall-times in the nested box-car sequence and the channel on which they occur define the time- and bin-coordinates of the separation shock foot. At times  $t = r_5$  and  $t = r_4$ , for example, the separation shock enters bins 5 and 4 from bins 6 and 5, respectively. This information provides two points in the separation shock foot history,  $X_s(t)$  — indicated by  $r_5$  and  $r_4$  in Fig. 2h. Due to the spatial resolution restrictions, the separation shock motion cannot be determined for  $r_5 < t < r_4$ . All that is known is that it stays in bin 5. It is assumed that the motion of the separation shock during this time is unidirectional and at constant speed. This assumption allows for the linear interpolation of the two time/bin coordinates,  $r_5$  and  $r_4$ , as shown in Fig. 2h. Similarly, another interpolation is performed from  $t = r_4$  to  $t = r_3$  (i.e., the time when separation shock enters bin 3 from bin 4). At time  $t = f_3$  the separation shock enters bin 4 from bin 3. In this case, a different linear interpolation is required since the separation shock changes its direction of motion within this time interval (i.e.,  $r_3 < t < f_3$ ). It is further assumed that the separation shock moves to the middle of the bin, changes its direction of motion and moves back at the same speed. This assumption results in the interpolation depicted in Fig. 2h. Those motions opposite of the ones discussed above (i.e., a sequence of fall-times and a fall-rise pair) are treated in a similar manner. Clearly, the linear interpolation yields a piecewise smooth function for  $X_s(t)$  as shown in Fig. 2h. It should be noted that the assumptions invoked in this derivation are not new and have always been implicit in conditional analysis techniques employed previously.

Once the separation shock position history,  $X_s(t)$ , is obtained, the separation shock velocity history,  $V_s(t)$ , can easily be calculated by taking the derivative of  $X_s(t)$ . The authors are aware of the problems involved in differentiating the experimental data, however, in this case  $V_s(t)$  can only be calculated by dividing the distance between two adjacent transducers by the time it takes for the shock to cross both transducers. Note that this is equivalent to differentiating  $X_s(t)$ . The corresponding velocity history is shown in Fig. 2i.

In the authors' opinion,  $X_s(t)$  and  $V_s(t)$  are the most comprehensive and accurate characterization of the unsteadiness in these interactions. Once they are determined,  $X_s(t)$  and  $V_s(t)$  are analyzed using standard time-series analysis techniques and are correlated with wall pressure measurements made upstream and downstream of the intermittent region or with other conditionally sampled signals obtained from wall pressure measurements in a given interaction.

### 3.3. Derivation of instantaneous pressure ratio history

In addition to  $X_s(t)$  and  $V_s(t)$ , it is also desirable to know the histories of the ratio of static pressures across the separation shock. To obtain this, one would ideally need an instrument which traveled with the separation shock. Clearly, it is not possible to make these measurements. However, an approximation of the static pressure ratio history can be obtained from simultaneous measurements of wall pressure fluctuations in the intermittent region.

To calculate the instantaneous pressure ratio across the separation shock,  $R_s(t)$ , one must first determine its position at that instant in time. Note that the separation shock position history,  $X_s(t)$ , has already been determined and is shown in Fig. 2h. At any time,  $R_s(t)$  is given by  $P_2(t)/P_1(t)$ , where  $P_2(t)$  are the pressure fluctuations measured by the transducer immediately downstream of the separation shock and  $P_1(t)$  are those fluctuations measured by the upstream transducer. As can be seen in Fig. 2h, the separation shock is in bin 5 from time  $t = r_5$  to  $t = r_4$ . During these times,  $P_1(t)$  and  $P_2(t)$  fluctuations are measured by channels 4 and 5, respectively, and  $R_s(t)$  is calculated from these pressure fluctuations. Similarly, for  $r_3 < t < f_3$  the separation shock is in bin 3, and  $R_s(t)$  is calculated from pressure fluctuations measured by channels 2 and 3. As a result of zero-drift problems, boundary layer pressure level,  $\bar{P}_{wo}$ , will differ from channel to channel. This can lead to inaccurate calculation of  $R_s(t)$ . Therefore, to avoid any bias in  $R_s(t)$ , measured  $\bar{P}_{wo}$  are first subtracted from upstream,  $P_1(t)$  and downstream,  $P_2(t)$  pressure fluctuations and freestream static pressure,  $P_\infty$ , is added to both. Corresponding pressure ratio fluctuations,  $R_s(t)$ , calculated from data shown in Figs. 2a through 2f, are plotted in Fig. 2j.

It should be noted that, when the separation shock is in bin 1,  $P_1(t)$  fluctuations are not known, and  $R_s(t)$  cannot be calculated. Similarly, when the shock is in bin 9,  $P_2(t)$  fluctuations are not known (see the schematic). Those times during which  $R_s(t)$  cannot be calculated are ignored in the analysis.

### 3.4. Variable interval cross-correlation

Cross-correlation of two simultaneously sampled signals is generally calculated using standard time-series analysis techniques. The data are first divided into equal interval records, which are Fourier transformed independently. The transformed results are then ensemble-averaged to give cross-spectral density function. The cross-correlation result is obtained by taking the inverse Fourier transform of the cross-spectral density function.

In some cases, particularly when conditional sampling analysis is used, it is necessary to work with variable interval data blocks. The Variable Interval Cross-Correlation algorithm has been developed for exactly this purpose. This algorithm performs an algebraic calculation of cross-correlation between two simultaneously sampled channels of data. In this method, the data from the first channel are divided into a certain number of blocks, each of which can be different in size. Each data block is then correlated with the corresponding data block extracted from the second channel. This is repeated for all data blocks and the final cross-correlation result is obtained by ensemble-averaging the individual cross-correlation results for each data block. To improve accuracy, the data block from the second channel is padded on both sides.

The results presented in this paper have been calculated using both the standard and the Variable Interval Cross-Correlation methods.

### 3.5. Digital filter

A Finite Impulse Response, FIR, digital filter has been used to examine band-limited correlations between separation shock dynamics (i.e.,  $X_s(t)$  and  $V_s(t)$ ) and other measurements. To do this, the signals were digitally filtered in either the low-pass or band-pass modes

prior to any analysis. Correlations of  $X_s(t)$  and  $V_s(t)$  with fluctuating pressure measurements were examined in frequency bands of 0-50 kHz, 0-3 kHz and 3-50 kHz. It should be noted that,  $V_s(t)$  was itself never filtered, instead the so-called filtered velocity fluctuations,  $V_s(t)$  were merely the derivative of the filtered  $X_s(t)$  signal. A piecewise smooth signal, such as , can be represented by the sum of an infinite series of sinusoids. When the signal is low-pass filtered, the result corresponds essentially to a truncated series of sinusoids. Consequently, the filtered signal displays the well known Gibbs phenomenon, however, the effect of these "ripples" is negligible for the types of analysis performed in this study.

### 3.6. CFD model

In addition to the analysis of the experimental data, some of the physical phenomena have been examined using an inviscid, quasi one-dimensional computational model. In this model, time-accurate one-dimensional Euler equations are used to solve supersonic/subsonic inviscid flow in a diverging channel. The inlet and outlet boundary condition were so prescribed to force a normal shock to occur in the mid-section of the channel. Once the steady-state solution was reached, the inlet and/or outlet boundary conditions were varied using sinusoidal perturbations whose amplitude and frequency could be controlled independently. The response of the normal shock to these perturbations was monitored by recording its position at each time step. Although this numerical model does not encompass all physical phenomena observed in experiments, it does nevertheless model the unsteadiness of a shock and convection of disturbances in an inviscid flow. It can, therefore, be used to show qualitatively how a shock will respond to perturbations in the boundary conditions.

It should be emphasized that, the authors do not claim to have modeled the physical phenomena observed in experiments. Instead, this CFD model has been introduced as a tool to examine some aspects of the unsteadiness observed in shock wave / turbulent boundary layer interactions. It will be shown later that the results obtained from this numerical analysis support one part of the mechanism of unsteadiness deduced from the analysis of the experimental data.

## 4. Discussion of Results

To recap, the objective of the current work is to examine the separation shock dynamics in several interactions and determine whether a universal model describing the unsteadiness can be developed. To do this, the unsteadiness is characterized in terms of separation shock position,  $X_s(t)$  and velocity,  $V_s(t)$  histories. These quantities have been correlated with conditionally sampled pressure-ratio fluctuations and wall pressure fluctuations measured upstream and/or downstream of the intermittent region. Before discussing the results of these correlations, some basic measurements describing these interactions will be presented first. Following the discussion of cross-correlation results, a model describing the physical causes of separation shock unsteadiness will be developed.

### 4.1. Mean, standard deviation, and intermittency distributions

Distributions of normalized mean wall pressure,  $\bar{P}_w / P_\infty$  are plotted versus the normalized distance,  $x/\delta_0$ , in Fig. 3a. It should be noted that  $\delta_0$  is not the appropriate normalizer in all cases. In fact, the data from the 25 deg swept compression ramp interaction should be plotted in the conical coordinate system (Erengil & Dolling 1993), and those from the blunt-fin interactions normalized by leading edge diameter. However, the intent here is to demonstrate the similarities and differences of the distributions from the unswept compression ramp

(UCR), the 25 deg swept compression ramp (SCR-25), the 8 deg swept blunt-fin (SBF-8), and the 30 deg swept blunt-fin (SBF-30) interactions. The separation lines,  $S$ , and upstream influence lines,  $UI$ , for the UCR and SBF-8 interactions are shown in Fig. 3a, and those for SCR-25 and SBF-30 are shown in Fig. 3b. As expected,  $\bar{P}_w / P_\infty$  distributions are similar in that they all increase gradually through the intermittent regions upstream of the compression corner or the blunt-fin root. Note that the spatial extent of the SBF-30 interaction is about one-third of the SBF-8 interaction. Similarly, the upstream influence of the SCR-25 interaction is smaller than that of the UCR interaction.

The normalized standard deviation,  $\sigma_{P_w}/P_\infty$ , distributions are plotted in Fig. 3b. Since the local maxima in these distributions are generated by the motion of the separation shock in the intermittent region, their magnitudes provide a measure of the strength of the separation shock. Based on the relative magnitudes of local maxima in  $\sigma_{P_w}/P_\infty$  shown in Fig. 3b, the separation shock has almost the same strength in the UCR and SBF-8 interactions whereas it is slightly weaker in the SBF-30 and SCR-25 interactions.

Finally, the intermittency distributions for these interactions are plotted in the same coordinates in Fig. 3c. Since the intermittency,  $\gamma$ , has a value between 0 and 1, the slope of these curves provides a simple measure of the length of the intermittent region. By visual inspection of the results in Fig. 3c, it can easily be concluded that the intermittent regions in the UCR and SBF-8 interactions are about the same length. The SBF-30 interaction has a smaller intermittent region and that in the SCR-25 interaction is the smallest.

#### 4.2. Power spectral densities of $X_s(t)$ and $V_s(t)$

Power spectral density coefficients of  $X_s(t)$  and  $V_s(t)$  are plotted in normalized form in Figs. 4a and 4b, respectively. These specific cases are identified in the legend in Fig. 4a, and for clarity, those results in Fig. 4b have been offset by the amounts indicated in its legend. When plotted in this form, the total area under the normalized distributions is unity, and the area within a frequency band represents the contribution to the variance from that frequency band.

As can be seen in Fig. 4a, there is practically no contribution to the variance of  $X_s(t)$  from frequencies in excess of about 10 kHz in any of these interactions. To verify that the transducer spacing does not impose a spatial filter on the  $X_s(t)$  signal, the authors used half as many transducers at double spacing to characterize the separation shock position history. There were few noticeable differences in the power spectral density distributions. Consequently, changes in the separation shock position occur at frequencies below 10 kHz in all these interactions. Clearly, dominant frequencies in  $X_s(t)$  increase progressively from about 0.2 kHz in the UCR interaction to about 3 kHz in the SCR-25 interaction. In the blunt-fin interactions, dominant frequencies in  $X_s(t)$  are between these two extremes and are higher in the SBF-30 interaction than they are in the SBF-8 interaction. Increasing dominant frequencies are consistent with decreasing intermittent region lengths (Gonzalez & Dolling 1993).

Several observations can be made from normalized power spectral density distributions shown in Fig. 4b. First, the sharp drop at 50 kHz is due to digital filtering of the separation shock position history,  $X_s(t)$ . As was mentioned earlier,  $V_s(t)$  is never filtered, and the so-called filtered velocity fluctuations are simply the derivative of the filtered  $X_s(t)$  signal. The effect of the digital filter could not be seen in Fig. 4a, because there is practically no energy in  $X_s(t)$  at frequencies above 50 kHz. Second, the frequency content of the velocity fluctuations is essentially broadband particularly in the UCR and SBF-8 interactions. In the SBF-30 interaction, the frequency distribution is bimodal with a dominant peak in the 3 to 4 kHz range. In the SCR-25 interaction, dominant frequencies are within the range of 4 to 5 kHz and very well

pronounced. Third, there is a gradual and a subtle trend towards higher frequencies in  $V_s(t)$  with decreasing intermittent region length.

To summarize, the results presented so far show the similarities and differences in all the interactions studied. As indicated by the mean results presented in Fig. 3, although their scales differ, these interactions all have a similar separation process. However, dominant frequencies characterizing the separation shock unsteadiness are quite different in each of these interactions.

#### 4.3. Correlation of $V_s(t)$ with pressure ratio fluctuations

For an unsteady shock wave, the governing equations can be reduced to an expression in which the shock speed is given by the ratio of static quantities across the shock, primarily the static pressure ratio. Hence, it is useful to examine whether there is a correlation between separation shock velocity,  $V_s(t)$  and conditionally sampled wall pressure ratio,  $R_s(t)$  histories. As was discussed earlier,  $R_s(t)$  can be derived from simultaneous measurements of multi-channel wall pressure fluctuations made in the intermittent region.

Normalized results of the correlation of  $V_s(t)$  and  $R_s(t)$  are shown in Fig. 5. For clarity, results from the SBF-8, SBF-30, and SCR-25 interactions have been offset as indicated in the figure. The negative correlation peak implies that *negative* fluctuations in separation shock velocity,  $V_s(t)$  correlate with *positive* fluctuations in wall pressure ratio,  $R_s(t)$  and vice versa. Furthermore, a negative time delay means that fluctuations in  $V_s(t)$  are *preceded* by those in  $R_s(t)$ . Thus an *increase* in the static pressure ratio across the separation shock causes a *decrease* in its velocity and vice versa. It should be noted that a change in separation shock velocity does not necessarily imply a change in its direction of motion — it simply means that the separation shock is either speeding up or slowing down. The direction of motion of the separation shock is given by the sign of its velocity, and in this case a negative velocity means that the separation shock is moving in the upstream direction and vice versa. The mechanism of unsteadiness, therefore, is an integral result of fluctuations in separation shock velocity, where positive shock velocities integrate to downstream excursions and vice versa. Finally, these results show that this mechanism is common to and identical in all interactions.

To the best of the authors' knowledge, these results provide the first experimental evidence of a cause-and-effect relationship between wall pressure fluctuations and the separation shock wave unsteadiness in these interactions. To reiterate, fluctuations in the static pressure ratio across the separation shock induce fluctuations in its velocity which in turn cause a change in separation shock position. It should be noted, however, that the separation shock unsteadiness described by this mechanism is the small-scale, jittery motion, since  $R_s(t)$  is obtained by "following" the separation shock. In other words, since this analysis focuses on those fluctuations in the vicinity of the separation shock foot, it cannot account for the large-scale, global motion of the separation shock. To determine the cause of the large-scale unsteadiness, separation shock dynamics must be correlated with upstream and downstream pressure fluctuations separately. These results and others are presented in the following sections.

#### 4.4. Correlation of $V_s(t)$ with upstream pressure fluctuations

Normalized results of the correlation of  $V_s(t)$  with upstream wall pressure fluctuations are shown in Fig. 6. For clarity, results from the SBF-8, SBF-30 and SCR-25 interactions have been offset as indicated in the figure. Note that the normalized coefficients for these correlations are much lower than those shown in Fig. 5. This is because the separation shock velocity fluctuations actually correlate with fluctuations in  $R_s(t)$ , and these may or may not be

affected by the upstream pressure fluctuations. Obviously, the static pressure ratio is also a function of the instantaneous value of the downstream pressure fluctuations.

Regardless, there is a correlation and the results show a positive peak at negative time delay. This suggests that a positive (negative) fluctuation in the upstream pressure *can* generate a negative (positive) fluctuation in static pressure ratio,  $R_s(t)$  which causes a positive (negative) fluctuation in  $V_s(t)$ . The peak in the SCR-25 interaction is the smallest, but this should be expected since this interaction is highly swept and some turbulent structures which cross over the upstream transducer will not reach the separation shock foot along the line of measurement which is perpendicular to the local separation line. These results are consistent with and support those presented in Fig. 5. In each of the blunt-fin interactions, there is also a secondary positive peak at an earlier time-delay. This is due to the strong recirculation present in blunt-fin interactions (Kleifges & Dolling 1993). Some turbulent structures which have crossed over the upstream transducer travel to the fin root and back, and generate a fluctuation in  $R_s(t)$  which in turn causes a fluctuation in  $V_s(t)$ .

To demonstrate this physical phenomenon further, wall pressure measurements made upstream and downstream of the intermittent regions of these interactions have been correlated with each other. Normalized results of these correlations are shown in Fig. 7. For clarity, the results from the SBF-8, SBF-30 and SCR-25 interactions have been offset as indicated in the figure. It should be noted that these results are obtained from actual wall pressure measurements and not from conditionally generated signals. In the UCR interaction there is only a single peak at positive time delay. This is because the turbulent structures which cross over the upstream transducer are convected through the intermittent region and also cross over the downstream transducer, but are not recirculated. A similar convective process is also evident in the SCR-25 interaction. Furthermore, the lower correlation magnitude suggests that some of the turbulent structures which have crossed over the upstream transducer are swept away before they reach the downstream transducer. It should be noted that differences in the timing of the primary peaks are a direct result of different spacings between the two transducers. In the SBF-8 and SBF-30 interactions there is a primary and a secondary peak at positive time delays. The primary peak is due to the turbulent structures which have crossed over the upstream transducer, convected through the intermittent region and also crossed over the downstream transducer. The secondary peak, on the other hand, is caused by those structures which are recirculated within the separation zone, because the time delay for each of these secondary peaks corresponds approximately to the time required for turbulent structures to travel to the root of the blunt-fin and back over the downstream transducer. In addition to spatial decay of turbulent structures, the lower correlation magnitude for the secondary peaks also suggests that only some of the structures are recirculated. Furthermore, the time difference between the two peaks indicates that the recirculating structures require longer time in the SBF-8 interaction than they do in the SBF-30 interaction. This is because the latter is a much smaller interaction than the former, as can be ascertained from Fig. 3.

To recap, the results presented in Fig. 6 indicate that correlation of velocity fluctuations with upstream pressure fluctuations are essentially the same for all the interactions studied. The secondary peaks in blunt-fin interactions reflect some characteristics unique to these interactions as explained above. Furthermore, although these results provide additional support for the mechanism developed from correlations presented in Fig. 5, they clearly do not correlate with the large-scale, global motion of the separation shock. In other words, turbulent fluctuations in the incoming boundary layer can only induce small-scale unsteadiness by generating fluctuations in the ratio of static quantities across the separation shock. Consistent with the approach outlined at the end of the previous section, results from correlation of separation shock dynamics and downstream pressure fluctuations, as well as others, are presented in the following section.

#### 4.5. Correlation of $V_s(t)$ with downstream pressure fluctuations

The interpretation of the correlation of separation shock velocity,  $V_s(t)$  and downstream pressure fluctuations is somewhat complicated, since these fluctuations are coupled. Normalized results of the correlation of  $V_s(t)$  and wall pressure fluctuations are plotted in Fig. 8 for all interactions studied. For clarity, the results from the SBF-8, SBF-30 and SCR-25 interactions have been offset as indicated in the figure. In all four cases, the downstream transducer is located at or just downstream of the separation line. Clearly, the results are different for different interactions. For the SCR-25 interaction, for example, there is a well defined positive peak at negative time-delay and a negative peak at positive time-delay. This means that, positive (negative) fluctuations in pressure precede positive (negative) fluctuations in velocity, and that negative (positive) fluctuations in velocity are followed by positive (negative) fluctuations in pressure. This implies that there is a cyclic relationship between separation shock velocity fluctuations and wall pressure measurements near the separation line.

Similar observations are also valid for the SBF-30, SBF-8, and UCR interactions, although the correlation peaks broaden and shift to consistently greater time delays. This implies that characteristic (or dominant) frequencies of this cyclic relationship between separation shock velocity and downstream pressure fluctuations shift progressively to lower frequency bands for the SBF-30, SBF-8, and UCR interactions, respectively. It should be noted that these trends are consistent with those observed in power spectral density coefficients of separation shock position,  $X_s(t)$  and velocity,  $V_s(t)$  histories. Furthermore, as the dominant frequencies of this cyclic relationship decrease, other correlation peaks around  $\tau=0$  become apparent in at least the UCR and SBF-8 interactions. These observations suggest that there are two different physical phenomena by which velocity fluctuations correlate with downstream wall pressure fluctuations, and that these phenomena have different characteristic frequencies. Therefore, to better understand the results of correlation between these fluctuations, the signals have been digitally filtered in low-pass and high-pass modes to examine contributions from different frequency bands.

Normalized correlation of band-pass filtered fluctuations are shown in Fig. 9 for these interactions. The cut-off frequencies were set at 3 and 50 kHz. Again, results from the SBF-8, SBF-30 and SCR-25 interactions have been offset for clarity. In this frequency band, the correlation results are qualitatively the same for all the interactions studied. The dominant peak in these correlations has a negative magnitude and occurs at negative time delay. This suggests that negative (positive) fluctuations in downstream pressure precede positive (negative) fluctuations in separation shock velocity. These results are entirely consistent with and provide additional support for the mechanism described in the discussion of correlations presented in Fig. 5. Note that a negative fluctuation in downstream pressure may generate a negative fluctuation in  $R_s(t)$  which causes a positive fluctuation in separation shock velocity. Similarly, a positive fluctuation in downstream pressure may increase the pressure ratio across the separation shock and thereby induce a negative velocity. The magnitude of these correlation peaks is smaller than those shown in Fig. 5, because not all positive (negative) fluctuations in downstream pressure will generate a positive (negative) fluctuation in  $R_s(t)$ . The other peaks in the correlation results are due to the strong coupling between fluctuations in downstream pressure and those in separation shock velocity as well as in position histories. It should be noted that separation shock strength increases as the shock moves downstream, and vice versa (Erengil & Dolling 1991a). Therefore, a positive (negative) fluctuation in separation shock velocity, which causes a downstream (upstream) motion, results in a stronger (weaker) shock, which in turn generates a positive (negative) fluctuation in downstream pressure. Clearly, the strong coupling between separation shock dynamics and downstream fluctuations make the interpretation of these results quite difficult.

To further examine flow dynamics in the downstream regions of these interactions, wall pressure measurements under the separated bubble have been correlated with each other. Normalized results of these correlations are shown in Fig. 10. Again, these results have been offset for clarity as indicated in the figure. To minimize the effect of shock unsteadiness on these results, care was taken in the analysis to ensure that no data were included in which the separation shock crossed over any of these transducers. Furthermore, the pressure signals were digitally filtered with the cut-off frequencies set at 3 and 50 kHz. This analysis, therefore, focuses on the turbulent fluctuations and the results represent the dynamics of turbulent structures. In the UCR interaction there is a positive peak occurring at positive time delay. This suggests that the turbulent structures are convected in the downstream direction, and if there is backflow, it is not strong enough to be detected by wall pressure measurements. In the SBF-8, SBF-30 and SCR-25 interactions, there are peaks at positive and negative time delays, indicating that turbulent structures are convected in both upstream and downstream directions in the separated region. These observations further support the correlation results presented in Fig. 9, and show clearly that turbulent structures can be convected upstream to the vicinity of the separation shock, change the ratio of the static quantities and thereby induce a fluctuation in the shock velocity,  $V_s(t)$ .

Normalized correlations of low-pass filtered fluctuations are shown in Fig. 11 for the UCR, SBF-8, SBF-30 and SCR-25 interactions. These results correspond to those presented in Fig. 8 except that they have been low-pass filtered at 3 kHz. These results have also been offset as indicated in the figure. In this frequency band, the results are qualitatively the same for all the interactions. They all have a positive peak at a negative time delay and a negative peak at a positive time delay. The difference is in the broadening of the peaks which suggests a progressive shift in dominant frequencies towards the lower end of the 0-3 kHz range with the lowest frequencies present in the UCR interaction. The peaks at negative time delay suggest that positive (negative) fluctuations in downstream pressure *precede* positive (negative) fluctuations in separation shock velocity, whereas those at positive time delay suggest that positive (negative) fluctuations in pressure *follow* negative (positive) fluctuations in velocity. Before describing this correlation, it will be helpful to note that the wall pressure levels at these downstream stations are higher when the separation shock is at the upstream end of the intermittent region and lower when it is at the downstream end (see also Fig. 12). Thus a shock motion in the upstream direction (i.e., a *negative* velocity) will be followed by an *increase* in pressure at the downstream station and vice versa. This is entirely consistent with negative peaks at positive time delays seen in Fig. 11. That there exist positive peaks at negative time delays suggest that this correlation is a cyclic process. In other words, a high downstream pressure level is followed by a shock motion in the downstream direction, which leads to a decrease in the downstream pressure level, which in turn is followed by a shock motion in the upstream direction, leading to an increase in the downstream pressure level. Clearly, this is a cyclic process which makes it difficult to establish a cause-and-effect relationship. However, it does suggest that there is a correlation between large-scale separation shock motion and expansion and contraction of the separation bubble, since an upstream motion of the shock corresponds to expansion of the bubble whereas a downstream motion corresponds to contraction of the bubble.

#### 4.6. Correlation of $X_s(t)$ with downstream pressure fluctuations

The mechanism suggested by the correlation between separation shock motion and expansion and contraction of the separation bubble is quite different from that dictated by the ratio of static quantities across the separation shock foot. In the latter, the shock motion is an integral result of velocity fluctuations caused by perturbations in the ratio of static quantities

across the shock. In the former, the separation shock, which forms immediately upstream of the separation bubble, is simply displaced by such physical processes as the expansion and contraction of the bubble. Thus in the former case, the relevant parameter characterizing the separation shock unsteadiness is its position and *not* velocity history. Therefore, it is  $X_s(t)$  which should be correlated with measurements quantifying the dynamics of expansion and contraction of the separation bubble. Following is a short discussion explaining how the expansion and contraction of the bubble can best be quantified by wall pressure measurements.

Figure 12 (Erengil & Dolling 1991a) shows ensemble-averaged pressure distributions for different separation shock positions in the intermittent region of the UCR interaction. The solid line is the overall time-averaged pressure distribution, and the dashed lines correspond to different shock positions as shown in the figure. The most upstream dashed line distribution, indicated by open square markers, corresponds to a large separation bubble, whereas that, indicated by filled diamond markers, corresponds to a small separation bubble. These distributions show that expansion and contraction of the separation bubble can be quantified by wall pressure measurements made in the vicinity of the separation line. It should be noted that this is the optimum location for monitoring expansion and contraction of the separation bubble, since measurements made under the separation bubble, say at  $x/\delta_0 = -0.5$  (see Fig. 12), are essentially independent of the size of the bubble, and those, say at 40% intermittency, cannot quantify the dynamics of the separation for 60% of the time because the transducer will be under the undisturbed boundary layer for these times.

Figure 13 shows normalized results of correlation between separation shock position,  $X_s(t)$  and wall pressure measurements near the separation line in the UCR, SBF-8, SBF-30 and SCR-25 interactions. For clarity, results from the SBF-8, SBF-30 and SCR-25 interactions have been offset as indicated in the figure. Note that these results represent correlations in the entire frequency range, that is 0 to 50 kHz. First, the results are qualitatively the same in all the interactions. The difference is in the broadening of the peaks which is also accompanied by a decrease in their magnitudes. As was discussed earlier, the broadening of the peaks indicates a decrease in the characteristic frequencies of the unsteadiness which is also characterized by power spectral density distributions of separation shock position histories shown in Fig. 4a. Most importantly, these correlations have a strong negative peak at negative time delay. This means that negative (positive) fluctuations in pressure *precede* positive (negative) fluctuations in separation shock position. It should be noted that higher levels of pressure near the separation line correspond to a larger separation bubble and vice versa (also see Fig. 12). Given this, the results presented in Fig. 13 show that the expansion of the separation bubble causes a shock motion in the upstream direction, whereas the contraction of the bubble results in a motion in the downstream direction.

#### 4.7. Physical model of the unsteadiness

Based on the experimental results presented in previous sections a physical model describing the separation shock unsteadiness in all four shock wave / turbulent boundary layer interactions can be constructed. In this model, separation shock motion, can be caused by two different physical phenomena which comprise the two parts of the mechanism. In the first part, the unsteadiness is caused by perturbations in the ratio of static quantities across the separation shock. The ratio of static pressure,  $P_2(t)/P_1(t)$ , for example, can be changed by fluctuations in  $P_2(t)$ ,  $P_1(t)$  or both. This, according to governing equations, will cause either an increase or a decrease in separation shock velocity, which in turn integrates to a change in its position. It should be noted that, fluctuations in other static quantities, such as the density and temperature, can also introduce perturbations to the equilibrium conditions, (i.e., the balance of the downstream and upstream conditions across the separation shock). Note that this is strictly

a local phenomenon and fluctuations in static quantities must travel to the vicinity of the separation shock to generate perturbations in the equilibrium conditions. In these flows, fluctuations are generally caused by turbulence, and can either propagate in the flow or be convected by turbulent structures to the vicinity of the separation shock. It should also be noted that, in separated interactions, a substantial part of the flow downstream of the shock can be subsonic and turbulent fluctuations can propagate or be convected in the upstream direction. These turbulent fluctuations generally occur at high frequencies and, therefore, can only induce high frequency fluctuations in the ratio of static quantities and thus the separation shock velocity. This part of the mechanism is identical in all interactions.

The second part of the mechanism is related to the dynamics of the separation bubble. In this part of the model, the separation bubble is considered as a "flexible" and "permeable" body of fluid which behaves as an extension of the shock generating geometry. The separation shock forms at the upstream end of the bubble. The expansion of the separation bubble, for example, displaces the separation shock to an upstream position, whereas the contraction of the bubble results in a displacement in the downstream direction. In addition to this, the trembling of the separation bubble can also cause changes in separation shock position. The characteristic frequencies of this unsteadiness of the separated flow are different in different interactions. Among other things, they depend on the size and the internal structure and dynamics of the separated flow. In general and in a given interaction, the larger the separated flow the lower the characteristic frequencies. However, the unsteadiness of a certain size separated flow from the UCR interaction, for example, is characterized by much lower frequencies than that of a comparable size separated flow from the SCR-25 interaction. This is because the internal structure and dynamics of the latter are quite different. In the SCR-25 interaction, the separated flow is actually a spiraling vortex rather than the nominally two-dimensional separation bubble in the UCR interaction. The unsteadiness of the spiraling vortex is mostly in the form of a trembling type motion occurring at high frequencies, whereas that of the latter is usually in the form of an expansion and contraction type motion occurring at much lower frequencies. The unsteadiness of the separated flow may be caused by such physical phenomena as the entrainment of turbulent structures, which would expand the bubble, or it could simply be a dynamic response of this "flexible" body of fluid to incoming boundary conditions. In the latter, a fuller incoming velocity profile would cause the separation to occur further downstream leading to a smaller separation bubble or a displaced bubble of the same size. Thus variations in the velocity profile of the incoming turbulent boundary layer can result in a different size separation bubble or in a "sliding" motion for the same size bubble. It should be noted that, although the physical mechanism describing the large-scale, global motion of the separation shock is the same for all the interactions (i.e., expansion and contraction of the bubble and/or its trembling), this mechanism is characterized by different frequencies in different interactions.

#### *4.8. Source of low-frequency component*

From the work described above, it is clear that the high-frequency, jittery motion of the separation shock is the result of the passage through the wave of individual large-scale turbulent structures. Thus, it is reasonable to conclude that this component of the unsteadiness is an inherent feature of all turbulent flows. The primary outstanding question concerns the cause of the low-frequency expansion/contraction of the separated flow which is characterized by the large-scale, long-duration excursions of the separation shock wave.

Preliminary experimental work to address this question has revealed two very interesting, complementary results. First, there is a distinct correlation between large-scale expansion or contraction of the separated flow and long duration (i.e., low-frequency) falls or rises in pitot pressure in the incoming turbulent boundary layer. In these experiments, fluctuating pitot

pressures were measured 9.28 inches ( $13.3\delta_1$ , where  $\delta_1$  = mass flux thickness) upstream of a compression ramp corner, while, at the same time, fluctuating wall pressures were measured within the intermittent region. Specific motions of the shock foot were then used as "triggers" for extraction of ensembles from the fluctuating pitot signal. Ensemble-average pitot pressure signals are presented in Fig. 14a for an upstream shock sweep and in Fig. 14b for a downstream shock sweep. Within the boundary layer ( $Y < 0.9\delta_1$ ), there is a well resolved decrease in pitot pressure while the shock is undergoing an upstream motion, and an increase in pitot pressure while the shock is undergoing a downstream motion. The time scale of these gradual rises and falls in pitot pressure is around 1 ms, almost two orders of magnitude higher than the large eddy time scale  $\delta_1/U_\infty$ . Thus, these rises and falls in pitot pressure are not generated by individual turbulent structures, but are caused by low-frequency "global" motion of the boundary layer. Second, results from the same experiment show that the ensemble-averaged pitot pressure at a fixed location in the incoming undisturbed boundary layer correlates with separation shock wave position. Three positions were considered: (1) shock foot at upstream edge of intermittent region (i.e., corresponding to large separation bubble), (2) shock foot at downstream edge of intermittent region (i.e., small separation bubble), and (3) shock foot centered within intermittent region. Results showed that the ensemble-average pitot pressure was below its overall mean value for case 1 (large bubble), above it for case 2 (small bubble), and equal to it for case 3.

These two sets of results suggest a model in which the boundary layer "thickens and thins" as it flows downstream (that is why, at a fixed point above the wall, the pitot pressure rises or falls). In such a simple model, a higher pitot pressure at a fixed height would imply a fuller velocity profile than the mean profile, one more resistant to separation, which would generate a smaller separation bubble than would the mean profile. Conversely, a lower pitot pressure at a fixed height would imply a slightly retarded profile which would generate a larger separation bubble than would the mean profile. Both observations are consistent with the experimental observations, as is the fact that, when the shock foot is at its mean position (case 3 above), the ensemble-averaged pitot pressure takes the overall mean value. However, at this stage it must be emphasized that the "thickening-thinning" boundary-layer model is an inference.

In speculating about possible causes of a thickening-thinning boundary layer, the question of Taylor-Gortler vortices arose. When a boundary layer develops on a concave wall, Gortler vortices can occur within the boundary layer (Fig. 15). A centrifugal force imposed by the curvature of the wall forces fluid particles to be displaced towards the wall. On the other hand the pressure force opposes this centrifugal force to restore the particles to their original position. When the centrifugal force is larger than the pressure force such that the viscosity cannot damp the motion, the flowfield is considered to be unstable and small disturbances are likely to be amplified. This is the underlying mechanism of the counter-rotating streamwise vortices, usually called "Gortler vortices." Although Gortler instability, which is inviscid in nature, has undergone many investigations, these investigations are mostly limited to laminar and incompressible flowfields with emphasis on their role in the transition process. The existence of these vortices in compressible, turbulent flowfields, and how far downstream of a region of concave curvature such vortices persist are less clear. For a detailed overview of current knowledge of the subject, readers are referred to the excellent recent reviews by Floryan and Saric (1994).

Earlier work (Hoffman *et al.* 1985) shows that vortices developing on a concave wall wander about preferred lateral positions and these positions are likely to be determined by nonuniformities in the oncoming flow. Although the spanwise wavelength is usually about *twice* the boundary layer thickness, the spacing and amplitude are functions of the initial disturbances. In his review, Floryan suggests that the nonuniformities in the boundary layer

lead to spanwise variations in time-averaged measurements which signal the presence of vortices. Although this opinion is widely accepted, the streamwise evolution of the vortices is a point of controversy. While some researchers (So *et al.* 1975; Prabhu *et al.* 1981) observe that these vortices decay, others (Hoffman *et al.* 1985; Smits *et al.* 1981) do not confirm this observation. Floryan states that a study by Smits *et al.* suggests that the vortices generated in the curved section of a wind tunnel persist almost *indefinitely* downstream in the straight section. They observed large spanwise variations in the time-averaged skin friction, streamwise and vertical velocity components and Reynolds stresses as well as the spanwise wandering of these quantities. In another study at Mach 5 with two different nozzle geometries, Beckwith and Holley (1981) investigated the onset of transition under extremely low incident disturbance levels. Their oil flow visualization results show clear streak patterns which indicate the existence of the Gortler vortices up to a certain unit Reynolds number which depends on the geometry of the nozzle. Above this Reynolds number they saw fine streak patterns which could be evidence of the vortices in turbulent flow and commented that either Gortler vortices persist far downstream in the turbulent flow or that the boundary layer there has some quasi-turbulent state.

A well-known effect of Gortler vortices is alteration of the velocity field (Fig. 16). The low speed fluid close to the wall will be carried up into a region of high velocity and consequently will cause a local decrease in the velocity of the flow (upwash). If the vortex pair rotates in the opposite direction, then the high speed fluid will be carried down to a low-speed region and will cause a local increase in the flow velocity (downwash). A common way to identify the existence of Gortler vortices is through surface flow patterns. Usually, a dark surface is covered with a thin layer of light-colored tracer material. The locations corresponding to a downward motion induced by the vortex pairs are determined by the black streaks which indicate an increase in shear stress. Conversely, light-colored streaks are indications of an upward motion and a decrease in shear stress. The spanwise distance between two neighboring streaks of the same color corresponds to one pair of counter-rotating vortices and defines the wavelength of the vortex system.

To understand whether such a vortex system might exist in the current facility, an experiment was conducted in which two transducers with fixed spacing were located at different spanwise locations. In the absence of any vortex system the cross correlation coefficients obtained from different pairs of transducers should be the same. If there is a vortex system then it is possible that differences would be observed at different spanwise locations on the wall. Fig. 17a shows the maximum cross correlation coefficient as a function of the spanwise location. Note that Z=3 inches is the centerline of the tunnel. There is clearly a systematic spanwise variation in the maximum cross correlation coefficient. There is strong evidence of periodicity with a wavelength of approximately *twice* the boundary layer thickness. This result suggests that Gortler vortices are present in the facility. A hypothetical vortex pair system based on the variations in the maximum cross correlation coefficient is also shown in Fig. 17b. Note that the local maximum value of  $R[0, \Delta Z, 0 | \tau]_{\max}$  corresponds to the region in which the low speed fluid is carried up into a high speed flow region. This result may implicitly be related to the variations in the wall shear stress ; when the shear stress is smaller, this will cause a decrease in the friction velocity,  $U_\tau$ . If inner scaling is used to plot the maximum spanwise cross correlation coefficient, it is evident that a decrease in  $U_\tau$  will effectively cause a decrease in the dimensionless parameter  $\Delta Z U_\tau / v_w$  for a fixed spanwise separation. This, in turn, will cause an effective increase in the maximum cross correlation coefficient.

Examination of the spanwise behavior of the rms of the fluctuations, and the skewness and flatness coefficients (Fig. 18a, 18b and 18c, respectively), does not reveal any obvious periodicity. As noted earlier there is quite a large uncertainty in the rms measurement which may mask small spanwise variations.

The spanwise variations in the displacement thickness,  $\delta^*$ , and the skin friction coefficient,  $C_f$ , obtained by Barter and Dolling (1993), are given in Fig. 19. Although it is difficult to reach a firm conclusion, it can be seen that there is a local maximum in  $\delta^*$  and local minimum in  $C_f$  very close to the center of the tunnel. The local minimum for  $\delta^*$  is approximately 0.7 inches to the left and right of the local maximum close to the center. This is followed by local maxima which yields a periodicity of approximately  $2\delta_0$ . Similar remarks can be made about the skin friction coefficient.

From the behavior of the maximum cross correlation, displacement thickness and skin friction coefficient, it might be inferred that the Gortler vortices exist in the test section. How these vortices affect the dynamics of shock-induced separation, if at all, is an interesting question. For close spacings, the spanwise cross correlation of wall pressure signals has the expected shape (Fig. 20), the time delay at maximum correlation is zero, and the decay of the maximum correlation coefficient is rapid at least for  $\Delta Z / \delta_0 \leq 1$ . All of this is consistent with pressure signals generated by large scale turbulent structures. Beyond  $\Delta Z / \delta_0$  of about 1, the decay is more gradual and at certain spacings unusual cross correlations are observed (i.e., Fig. 21). Non-zero time delays such as those in Fig. 21 must be caused by structures, or other pressure generating mechanisms, oblique to the flow direction. No proof can be offered at this stage but the question arises as whether the gradual decay of the cross correlation coefficient and results of Fig. 21 could be related to the spanwise wandering of Gortler vortices about their preferred positions, which in turn also affect the shock foot motion.

#### 4.9. Results from computational analysis

To examine the validity of the first part of the physical model developed from experimental results, a computational analysis has also been performed. In this study, time-accurate Euler equations governing the inviscid flow in a quasi one-dimensional channel have been solved using the Van Leer flux-vector splitting scheme (Van Leer *et al.* 1987). The inlet and outlet boundary conditions were so prescribed to cause the formation of a normal shock in the middle of the channel for the steady-state solution. The channel geometry, and the Mach number and static pressure distributions for the steady-state solution are plotted in Figs. 22a, 22b, and 22c, respectively. Since the convergence criterion was based on a global average-error calculation, the shock is smeared over a couple of cells. For the purposes of this study, this is not important. Once the steady-state solution converged, the static pressures at the inlet and outlet boundary conditions were varied sinusoidally using the summation of four different sinusoids. This permits different perturbations by changing the amplitude and frequency of each of the four sinusoids. Typical pressure disturbance histories introduced at the inlet and outlet are plotted in Figs. 23a and 23b, respectively. The response of the normal shock to these perturbations was monitored by calculating its position (i.e., the cell in which it occurs) in the channel at each time step. Since the size of the cells dictates the spatial resolution by which the shock position can be determined, a simple linear interpolation has been used to yield a piecewise smooth normal shock position history,  $X_c(t)$ . The normal shock velocity history,  $V_c(t)$  can be calculated by simply taking the temporal derivative of its position history,  $X_c(t)$ . The normal shock position and velocity histories, corresponding to the disturbances shown in Figs. 23a and 23b, are plotted in Figs. 23c and 23d, respectively. The static pressure ratio across the normal shock,  $R_c(t)$  is also calculated at each time step. If the normal shock is in cell  $i$ , for example, then the upstream,  $p_u(t)$ , and downstream,  $p_d(t)$ , static pressures are calculated from the conservative variables in cells  $i-2$ , and  $i+2$ , respectively. The data from cells immediately upstream ( $i-1$ ) and downstream ( $i+1$ ) of the shock were not used for this calculation,

since the shock is smeared over a couple of cells as mentioned earlier. The static pressure ratio history generated by the inlet and outlet disturbances is plotted in Fig. 23e.

Once sufficient amounts of data for the normal shock velocity,  $V_c(t)$  and static pressure ratio,  $R_c(t)$  fluctuations were collected, the process was stopped. These data were then correlated using the variable interval cross-correlation method described earlier. The normalized results of this correlation are shown in Fig. 24. This correlation has a very strong negative peak which occurs at a negative time delay. This shows very clearly that fluctuations in the static pressure ratio across the normal shock cause opposite fluctuations in its velocity (also see Figs. 23d and 23e). Furthermore, the very strong correlation coefficient suggests that this is the *only* physical mechanism responsible for the normal shock oscillations in the channel.

Even though these results are from a quasi one-dimensional analysis, they nevertheless demonstrate the unsteadiness caused by fluctuations in the ratio of static quantities as dictated by the governing equations. This analysis, therefore, provides computational support for the first part of the physical mechanism developed from experimental results, as can be seen by comparing the results presented in Fig. 5 with those in Fig. 24.

## 5. Conclusions

The purpose of this work was (i) to examine separation shock unsteadiness in different interactions and determine whether a universal model describing the unsteadiness could be developed, and (ii) to determine whether or not the observed unsteadiness is a feature of turbulent flows in general, or is specific to the wind tunnel environment. To this end, wall pressure and pitot pressure fluctuation measurements were made in interactions generated by unswept and 25 deg swept compression ramp models, and by 8 deg and 30 deg swept blunt-fin models in a high Reynolds number, Mach 5 turbulent boundary layer. Using a new conditional sampling algorithm, the separation shock unsteadiness was characterized in terms of its position,  $X_s(t)$  and velocity,  $V_s(t)$  histories. These fluctuations were then correlated with the conditionally extracted static pressure ratio,  $R_s(t)$  across the separation shock, and with wall pressure measurements made upstream and downstream of the intermittent region in each of these interactions. A comprehensive physical model describing the unsteadiness has been developed. In this model, the separation shock unsteadiness can be caused by two different physical phenomena which comprise the two parts of the mechanism.

In the first part, the small-scale or jittery motion of the separation shock is caused by fluctuations in the ratio of static quantities across the shock foot. These perturbations induce fluctuations in the separation shock velocity and thus changes in separation shock position are an integral result of the velocity fluctuations. An increase in the ratio of static pressure, for example, causes an upstream excursion in the separation shock position and vice versa. The ratio of static quantities can be changed by independent fluctuations in upstream and downstream conditions or both. These fluctuations are attributed to turbulence and can either propagate or be convected to the vicinity of the separation shock.

In the second part, the large-scale or global motion of the separation shock is caused by the expansion and contraction or trembling motion of the separation bubble. Here, the separation bubble is considered as a “flexible” and “permeable” body of fluid which behaves as an extension of the shock generating geometry. The separation shock forms at the upstream end of the bubble. Thus, an expansion of the separation bubble, for example, displaces the separation shock to an upstream position, whereas a contraction of the bubble results in a displacement in the downstream direction. The unsteadiness of the separation bubble may be caused by such physical phenomena as the entrainment of turbulent structures, which would expand the bubble, or it could simply be a dynamic response of this “flexible” body of fluid to incoming boundary conditions. Thus variations in the velocity profile of the incoming turbulent boundary layer can result in a different size separation bubble or in a “sliding” motion for the

same size bubble. It should be noted that some evidence has been found of Taylor-Gortler vortices in the incoming flow, and it is possible that these play a role in the low-frequency physics. Confirmation using intrusive instrumentation alone is extremely difficult, and, in the next phase of the work, both conventional instrumentation and planar laser imaging methods will be used to explore the incoming flow structure corresponding to different separated bubble sizes and dynamics.

In addition to experimental results, computations in an inviscid, unsteady flow have also been performed. In this study, the response of a normal shock in a quasi one-dimensional channel was examined as perturbations in upstream and downstream boundary conditions were introduced. Although this does not model the experimental conditions, the results clearly demonstrate the unsteadiness caused by fluctuations in the ratio of static quantities as dictated by the governing equations. This analysis, therefore, provides computational support for the first part of the physical mechanism developed from experimental results.

## **6. Listing of Participating Scientific Personnel & Advanced Degrees Awarded**

- a) Dr. David S. Dolling, Principal Investigator
- b) Dr. Richard Gramann, Co-Principal Investigator
- c) Dr. Mehmet Erengil, Graduate Research Assistant, awarded Ph.D. in December 1993
- d) Haldun Unalmis, Graduate Research Assistant, will be awarded Ph.D. in May 1995
- e) Jack Barter, Graduate Research Assistant, will be awarded Ph.D. in May 1995

*Note: Dr. Erengil and H. Unalmis have worked consistently on the project over its duration. Jack Barter has received partial funding to participate in specific areas of the work as needed*

## **7. Listing of All Publications & Technical Reports**

- 1) "Unsteadiness of Shock-Induced Turbulent Boundary Layer Separation—an Inherent Feature of Turbulent Flow or Solely a Wind Tunnel Phenomenon," D. S. Dolling & M. E. Erengil, Final Report, August 1994.
- 2) "Decay of Wall Pressure Field and Structure of a Mach 5 Adiabatic Turbulent Boundary Layer," O. H. Unalmis & D. S. Dolling, AIAA Paper 94-2363, June 1994.
- 3) "Physical Causes of Separation Shock Wave Unsteadiness in Shock Wave Turbulent Boundary Layer Interactions," M. E. Erengil, Ph.D. dissertation, Dept. of Aerospace Engineering and Engineering Mechanics, Dec. 1993.
- 4) "Physical Causes of Separation Shock Unsteadiness in Shock-Wave/Turbulent Boundary Layer Interactions," M. E. Erengil & D. S. Dolling, AIAA Paper 93-3134, July 1993.
- 5) "Effects of Sweepback on Unsteady Separation in Mach 5 Compression Ramp Interactions," M. E. Erengil & D. S. Dolling, *AIAA Journal*, Vol. 31, No. 2, pp. 302–311, Feb. 1993.
- 6) "Fluctuating Loads in Shock Wave/Turbulent Boundary Layer Interaction: Tutorial and Update," D. S. Dolling, AIAA Paper 93-0284, Jan. 1993.
- 7) "Effects of Sweepback on the Dynamics of Unsteady Separation in Mach 5 Compression Ramp Interactions," M. E. Erengil & D. S. Dolling, AIAA Paper 92-0430, Jan. 1992.
- 8) "Examination of Turbulent Structures Associated with Unsteady Shock Motion in a Mach 5 Interaction," R. G. Gramann & D. S. Dolling, AIAA Paper 92-0744, Jan. 1992.

## REFERENCES

ANDREOPoulos, J. & MUCK, K. C. 1987 Some new aspects of the shock-wave / boundary-layer interaction in compression ramp flows. *J. Fluid Mech.* **180**, 405.

BARTER, J. W. & DOLLING, D. S. 1993 Experimental study of the use of vortex generators to reduce fluctuating pressure loads in shock wave turbulent boundary layer interactions. *AIAA Paper 93-4335*.

BECKWITH, I. E. & HOLLEY, B. B. 1981 Gortler vortices and transition in wall boundary layers of two Mach 5 nozzles. NASA Technical Paper 1869.

BOGDONOFF, S. M. 1955 Some experimental studies of the separation of supersonic turbulent boundary layers. Dept. of Aeronautical Engineering, Princeton University, Princeton, NJ, Rep. 336.

BRUSNIAK, L. & DOLLING, D. S. 1993 Flowfield dynamics in blunt-fin-induced shock wave / turbulent boundary layer interaction. *AIAA Paper 93-3133*.

CHAPMAN, D. R., KUEHN, D. M. & LARSON, H. K. 1958 Investigation of separated flows in supersonic and subsonic streams with emphasis on the effect of transition. NACA Report 1356.

DOLLING, D. S. & BRUSNIAK, L. 1989 Separation shock motion in fin, cylinder, and compression ramp-induced turbulent interactions. *AIAA J.* **27**, 734.

DOLLING, D. S. & SMITH, D. R. 1989 Separation shock dynamics in Mach 5 turbulent interactions induced by cylinders. *AIAA J.* **27**, 1698.

DOLLING, D. S. 1992 Problems in the validation of CFD codes through comparison with experiment. *AGARD Symposium on Theoretical and Experimental Methods in Hypersonic Flows, Turin, Italy*.

DOLLING, D. S. 1993 Fluctuating loads in shock wave / turbulent boundary layer: Tutorial and update. *AIAA Paper 93-0284*.

ERENGIL, M. E. & DOLLING, D. S. 1991a Unsteady wave structure near separation in a Mach 5 compression ramp interaction. *AIAA J.* **29**, 728.

ERENGIL, M. E. & DOLLING, D. S. 1991b Correlation of separation shock motion and pressure fluctuations in the incoming boundary layer. *AIAA J.* **29**, 1868.

ERENGIL, M. E. & DOLLING, D. S. 1993 Effects of sweepback on unsteady separation in Mach 5 compression ramp interactions. *AIAA J.* **31**, 302.

FLORYAN, J. M. 1991 On the Gortler instability of boundary layers. *Progress in Aerospace Sciences* **128**, 235–271.

GONSALEZ, J. C. & DOLLING, D. S. 1993 Correlation of interaction sweepback effects on the dynamics of shock-induced turbulent separation. *AIAA Paper 93-0776*.

GRAMANN, R. A. 1989 Dynamics of separation and reattachment in a Mach 5 unswept compression ramp flow. Ph. D. dissertation, Department of Aerospace Engineering and Engineering Mechanics, The University of Texas at Austin, Austin, TX.

GRAMANN, R. A. & DOLLING, D. S. 1992 Examination of turbulent structures associated with unsteady shock motion in a Mach 5 interaction. *AIAA Paper 92-0744*.

HOFFMANN, P. H., MUCK, K. C. & BRADSHAW, P. 1985 The effects of concave surface curvature on turbulent boundary layers. *J. of Fluid Mech.* **161**, 371–403.

KISTLER, A. L. 1964 Fluctuating wall pressure under separated supersonic flow. *J. Acoust. Soc. Am.* **36**, 543.

KLEIFGES K. & DOLLING, D. S. 1993 Control of unsteady shock-induced turbulent boundary layer separation upstream of blunt fins. *AIAA Paper 93-3281*.

KUSSOY, M. L., BROWN, J. D., BROWN, J. L., LOCKMAN, W. K. & HORSTMAN, C. C. 1987 Fluctuations and massive separation in three dimensional shock wave / boundary layer interactions. *2nd International Symposium of Transport Phenomena in Turbulent Flows, Tokyo, Japan*.

MARSHALL, T. A. & DOLLING, D. S. 1992 Comments on the computation of supersonic, unswept, turbulent compression ramp interactions. *AIAA J.* **30**, 2056.

McCLURE, W. B. 1992 An experimental study of the driving mechanism and control of the unsteady shock-induced turbulent separation in a Mach 5 compression corner flow. Ph. D. dissertation, Department of Aerospace Engineering and Engineering Mechanics, The University of Texas at Austin, Austin, TX.

PRABHU, A. & RAO, B. N. S. 1981 Effect of concave streamline curvature on turbulent boundary layers. *AIAA Paper* 81-1193.

ROBINSON, S. K. 1988 Effects of Riblets on turbulence in a supersonic boundary layer. *AIAA Paper* 88-2526.

SARIC, W. S. 1994 Gortler vortices. *Annual Review of Fluid Mech.* **26**, 379–409.

SMITS, A. J., YOUNG, S. T. & BRADSHAW, P. 1979 The effects of short regions of high surface curvature on turbulent boundary layers. *J. of Fluid Mech.* **94**, 209–242.

SO, R. M. C. & MELLOR, G. L. 1975 Experiment on turbulent boudary layers on a concave wall. *Aeronaut. Q.* **26**, 25–40.

SELIG, M. S. & SMITS, A. J. 1991 Effect of periodic blowing on attached and separated supersonic turbulent boundary layers. *AIAA J.* **29**, 1651.

TRAN, T. T. 1986 An experimental investigation of unsteadiness in swept shock wave / turbulent boundary layer interactions. Ph. D. dissertation, Mechanical and Aerospace Engineering Department, Princeton University, Princeton, NJ.

VAN LEER, B., THOMAS, J. L., ROE, P. L., & NEWSOME, R. W. 1987 A comparison of numerical flux formulas for the Euler and Navier-Stokes equations. *AIAA Paper* 87-1104-CP.

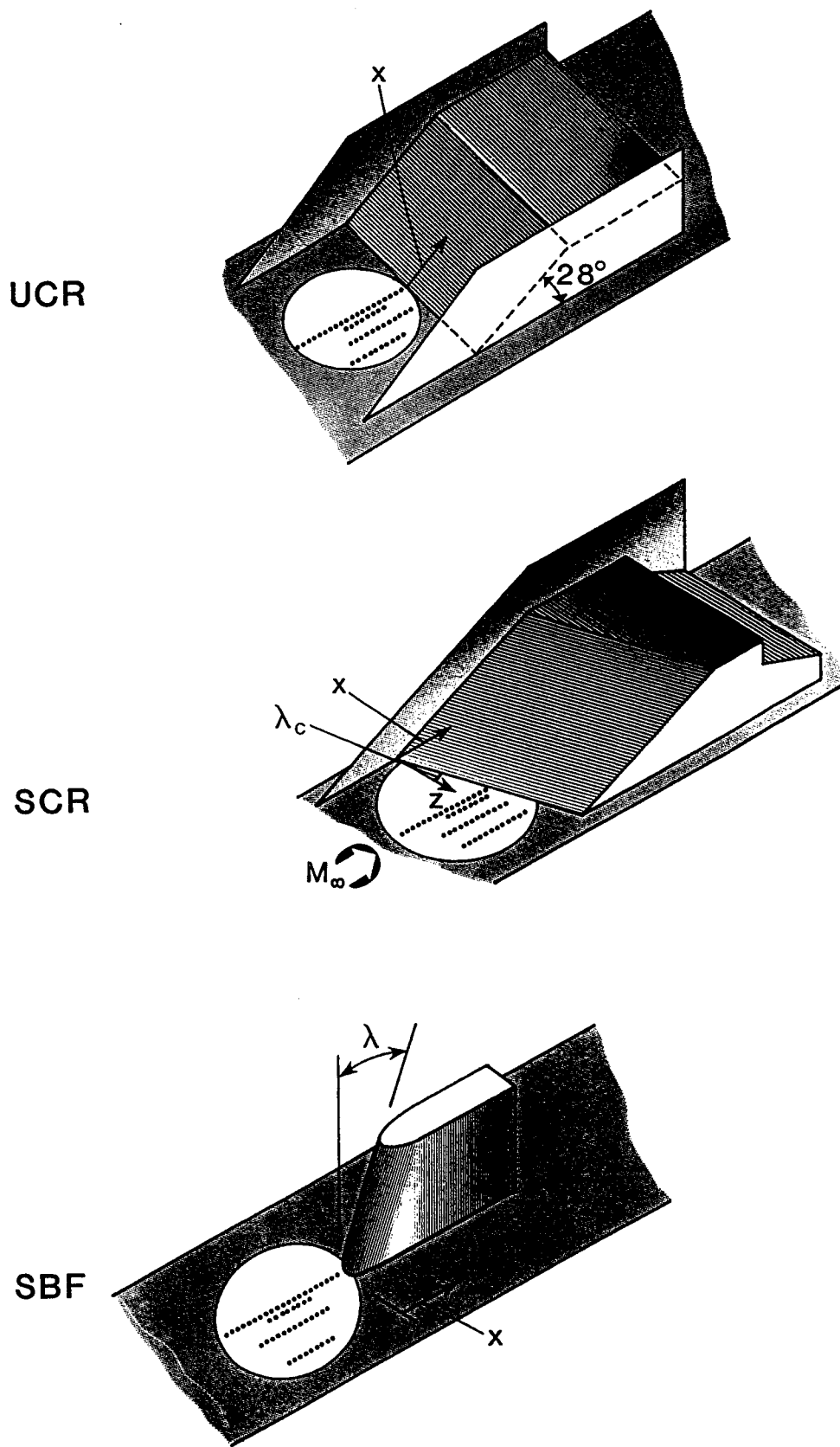


Fig. 1 Unswept and Swept Compression Ramp, and Swept Blunt-Fin Models

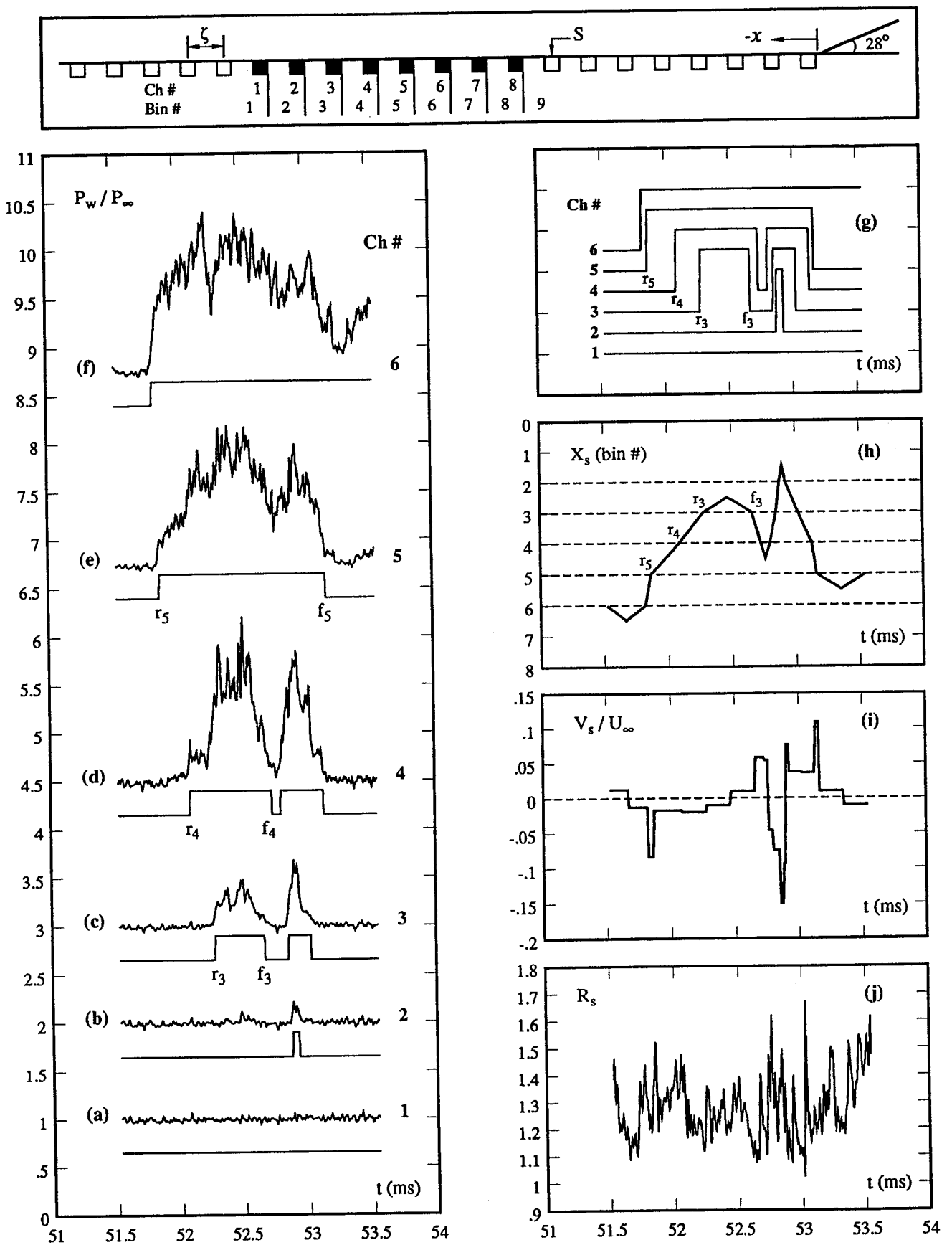


Fig. 2 Derivation of Shock Position,  $X_s(t)$ , Velocity,  $V_s(t)$ , and Pressure Ratio,  $R_s(t)$  Histories

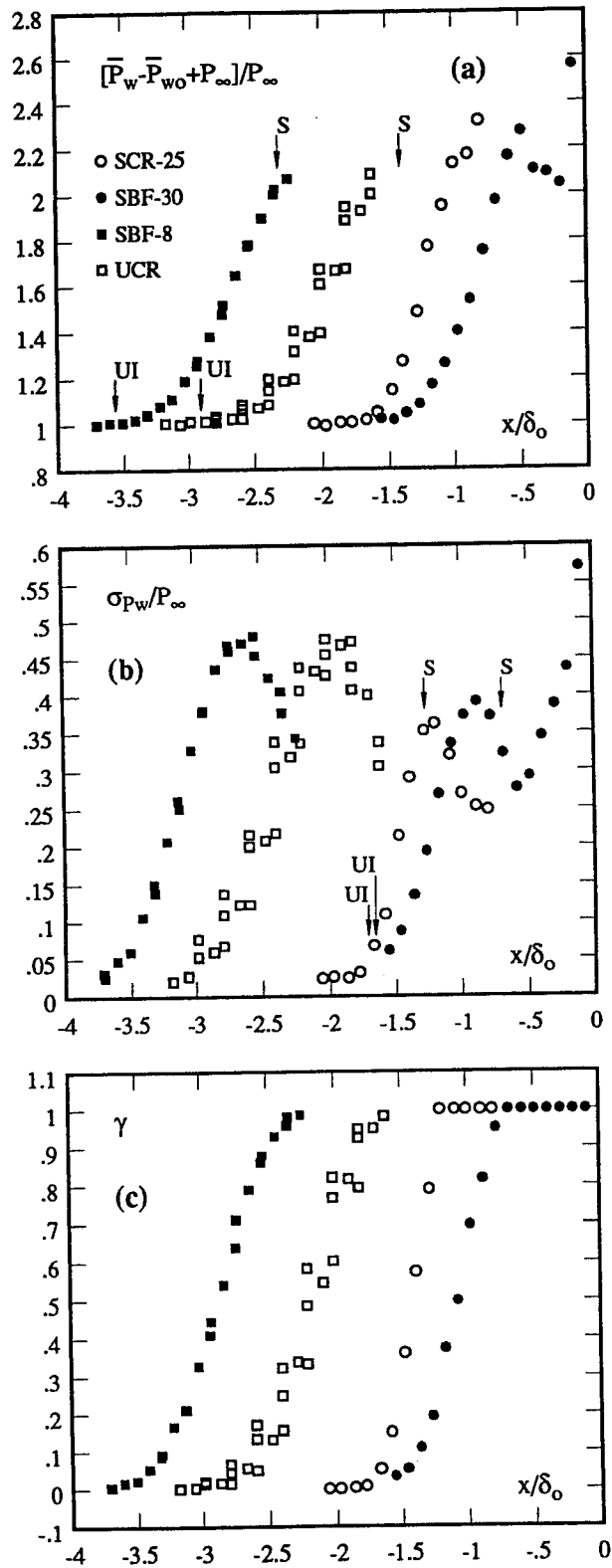


Fig. 3 Normalized Distributions of Mean,  
Standard Deviation, and Intermittency

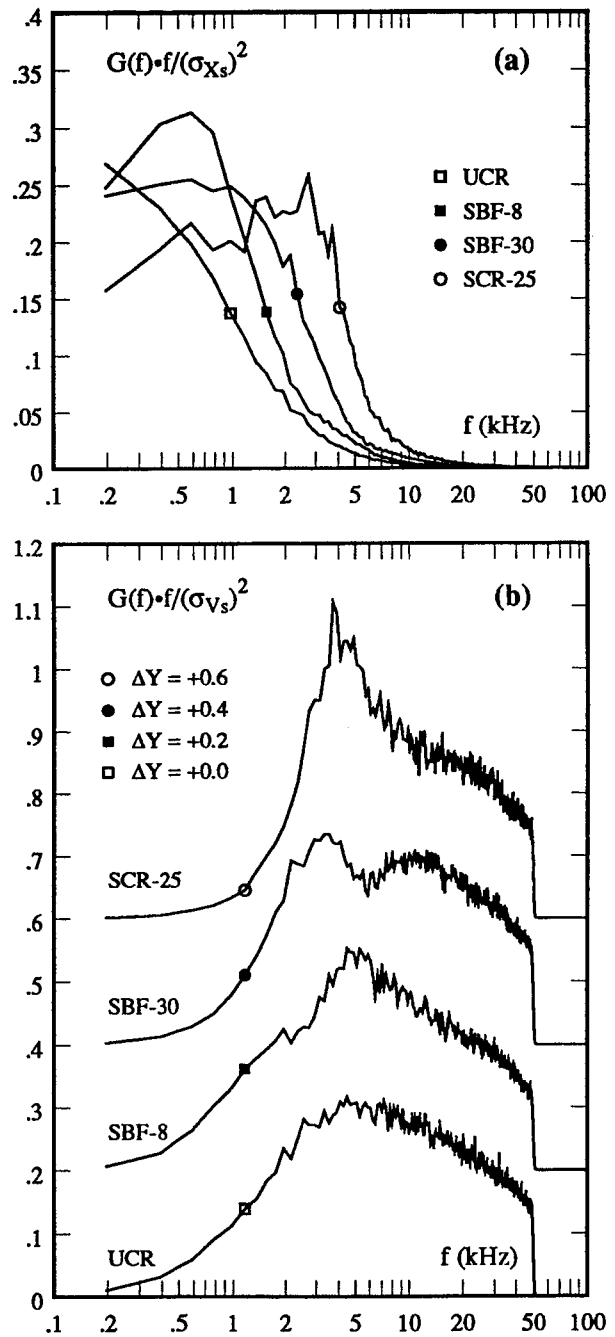


Fig. 4 Normalized Power Spectral Densities for Separation Shock Position,  $X_s(t)$ , and Velocity,  $V_s(t)$  Histories

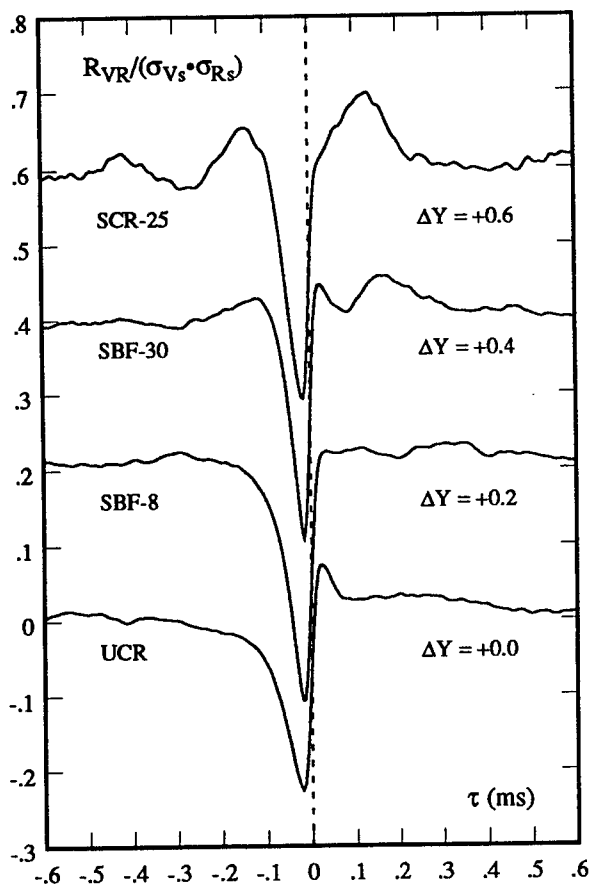


Fig. 5 Normalized Cross-Correlation of Shock  
Velocity,  $V_s(t)$ , and Pressure Ratio,  $R_s(t)$

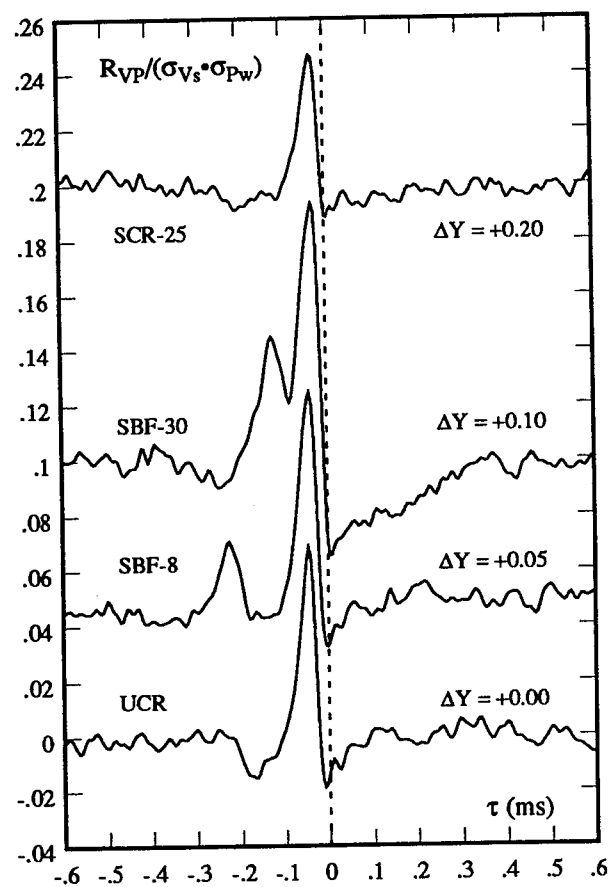


Fig. 6 Normalized Cross-Correlation of Shock  
Velocity,  $V_s(t)$ , and Upstream Pressure,  $P_w(t)$

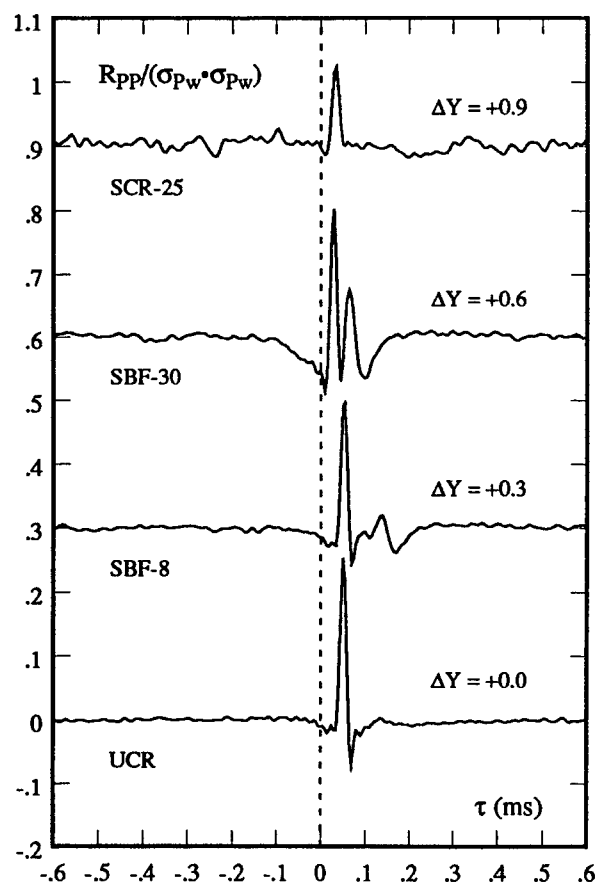


Fig. 7 Normalized Cross-Correlation of Upstream and Downstream Pressure Measurements

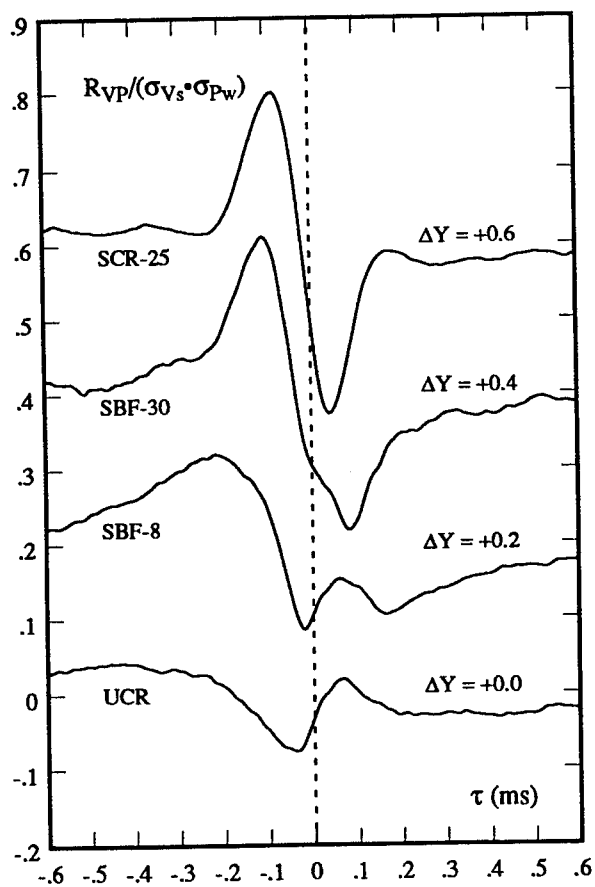


Fig. 8 Normalized Cross-Correlation of Shock Velocity,  $V_s(t)$ , and Downstream Pressure,  $P_w(t)$

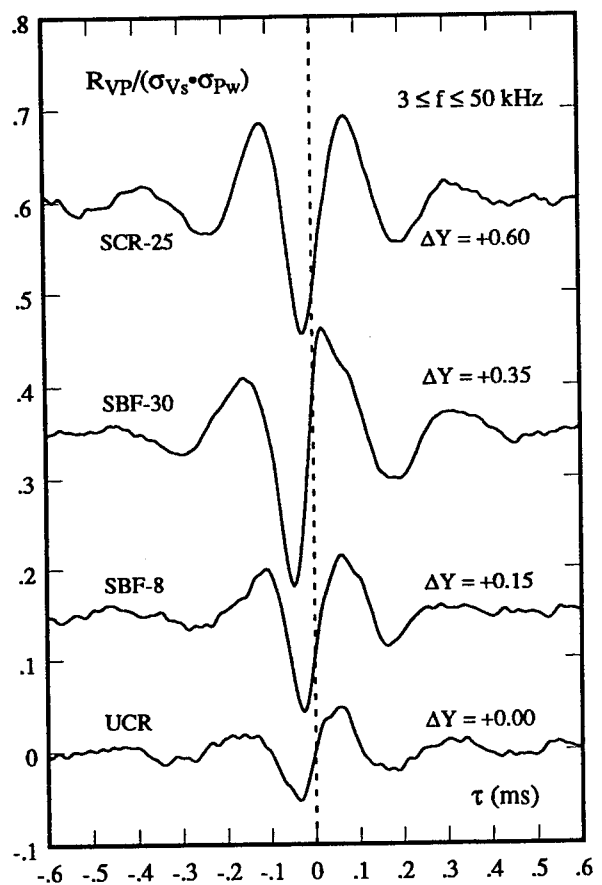


Fig. 9 Normalized Cross-Correlation of Shock Velocity,  $V_s(t)$ , and Downstream Pressure,  $P_w(t)$  (High-Pass Filtered,  $3 \leq f \leq 50$  kHz)

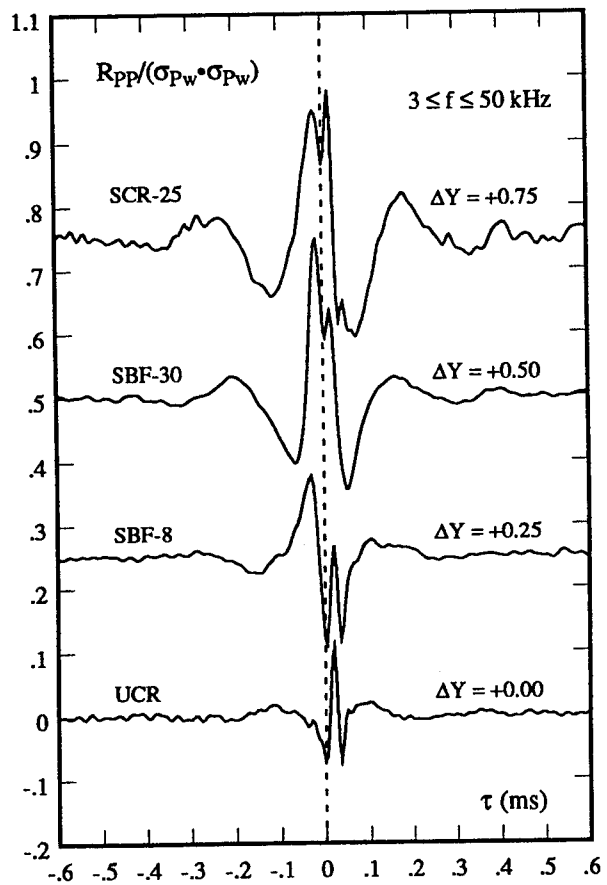


Fig. 10 Normalized Cross-Correlation of  
Downstream Pressure Measurements  
(High-Pass Filtered,  $3 \leq f \leq 50$  kHz)

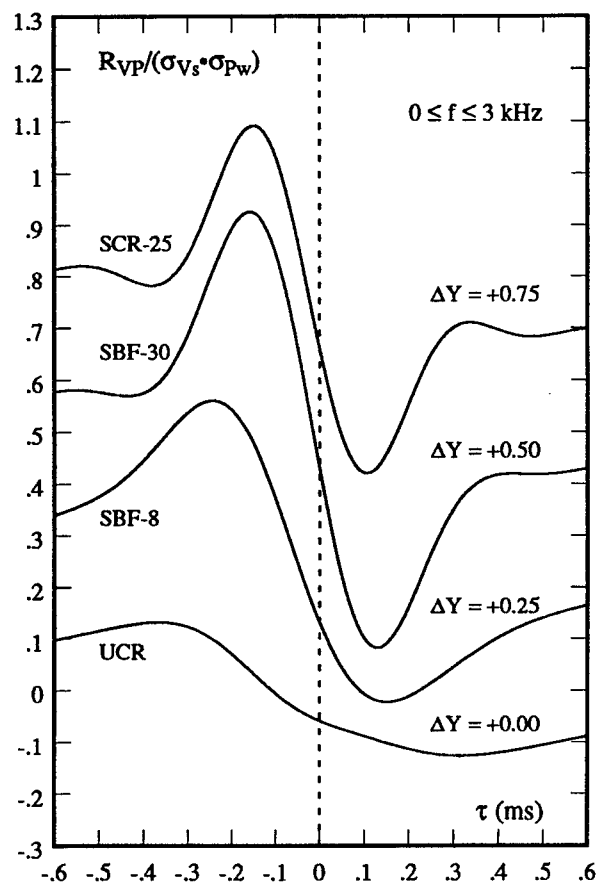


Fig. 11 Normalized Cross-Correlation of Shock Velocity,  $V_s(t)$ , and Downstream Pressure,  $P_w(t)$  (Low-Pass Filtered,  $0 \leq f \leq 3 \text{ kHz}$ )

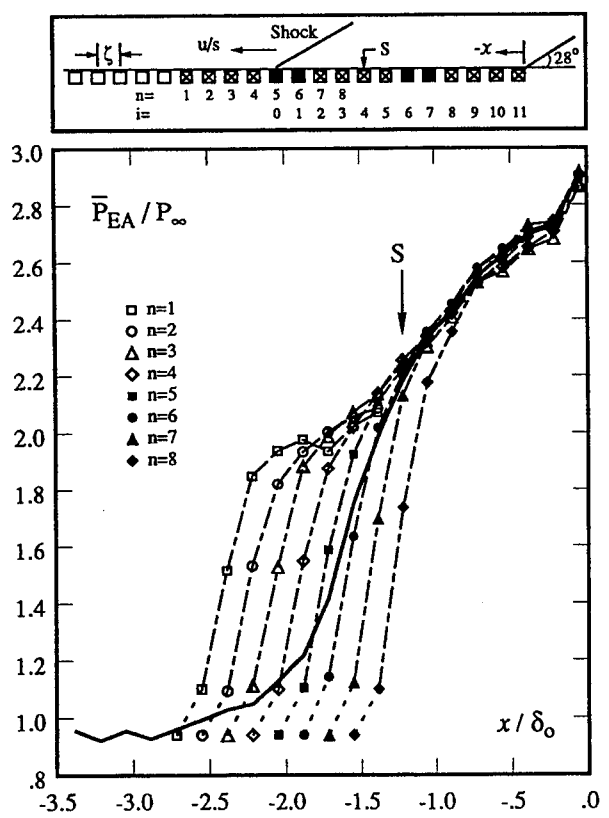


Fig. 12 Normalized Distributions of Ensemble-Averaged Pressure Measurements (Erengil & Dolling 1991a)

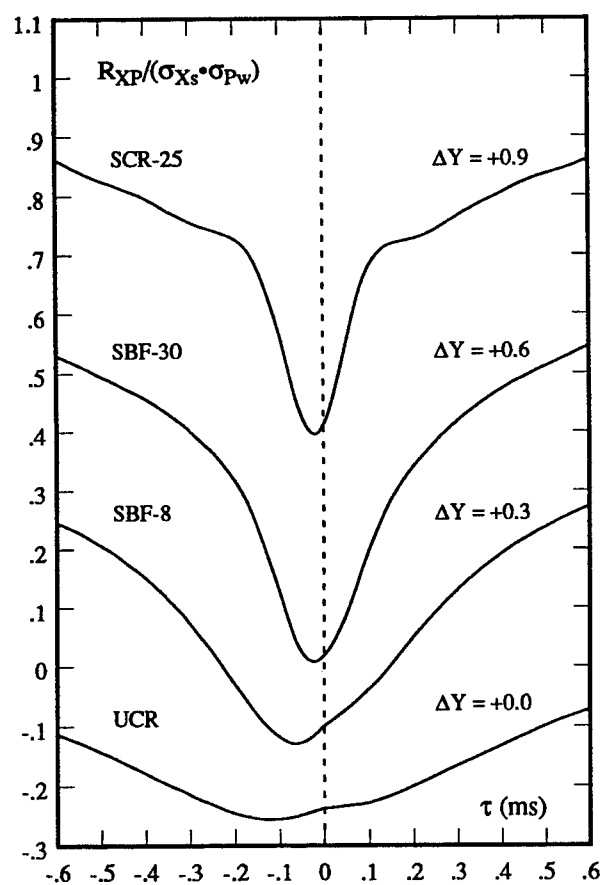


Fig. 13 Normalized Cross-Correlation of Shock Position,  $X_s(t)$ , and Downstream Pressure,  $P_w(t)$

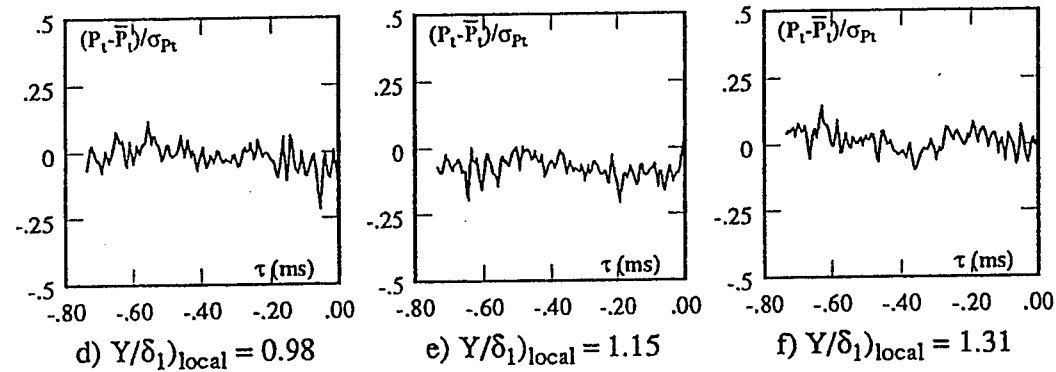
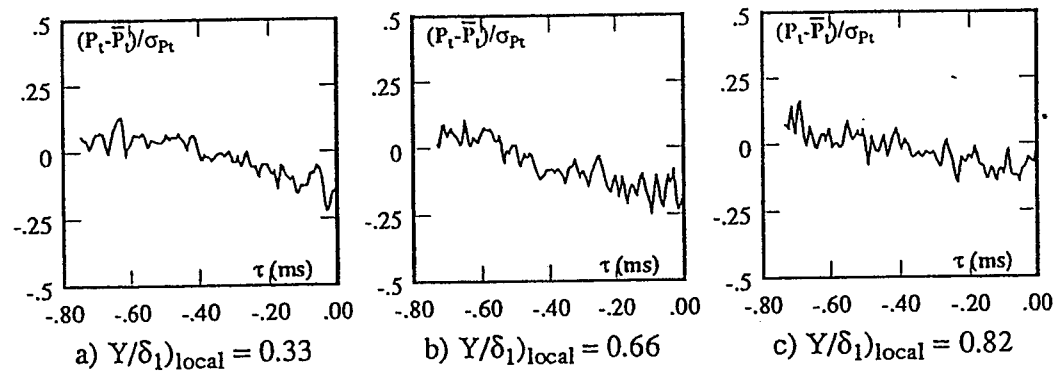
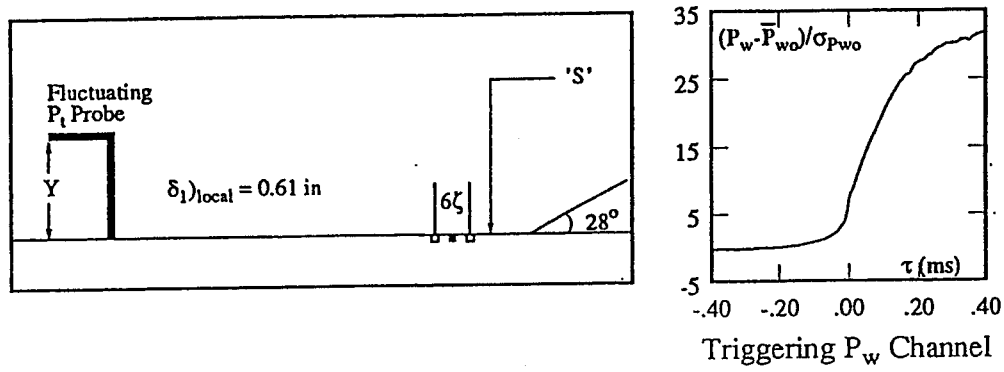


FIGURE 14a. Ensemble-averaged pitot pressure signals in the incoming boundary layer for an upstream shock sweep.

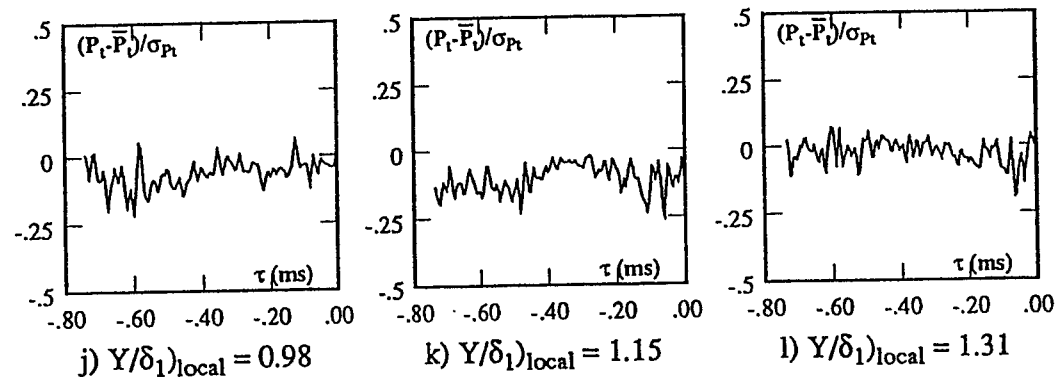
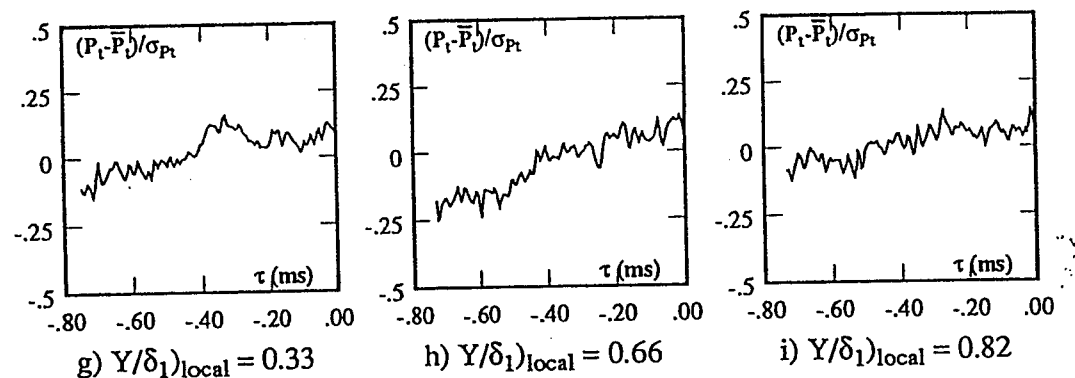
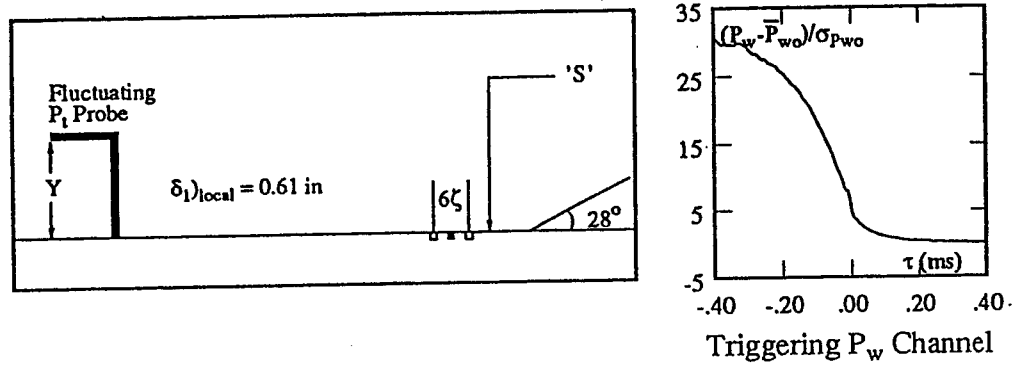


FIGURE 14b. Ensemble-averaged pitot pressure signals in the incoming boundary layer for a downstream shock sweep.

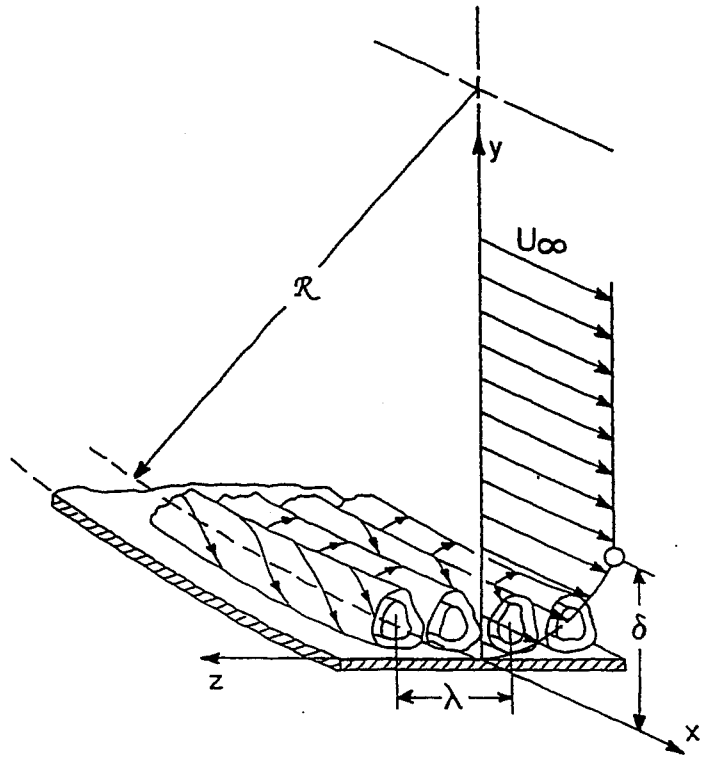


FIGURE 15. Gortler vortices in the boundary layer on a concave wall.

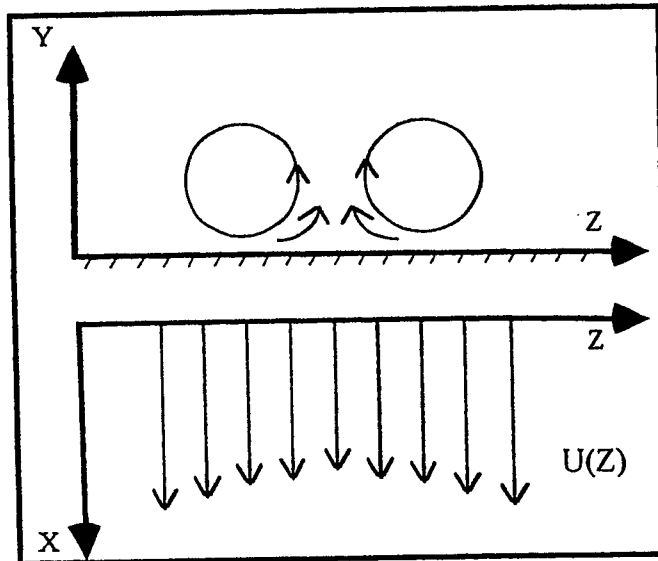


FIGURE 16. Alteration of streamwise velocity field by a vortex pair.

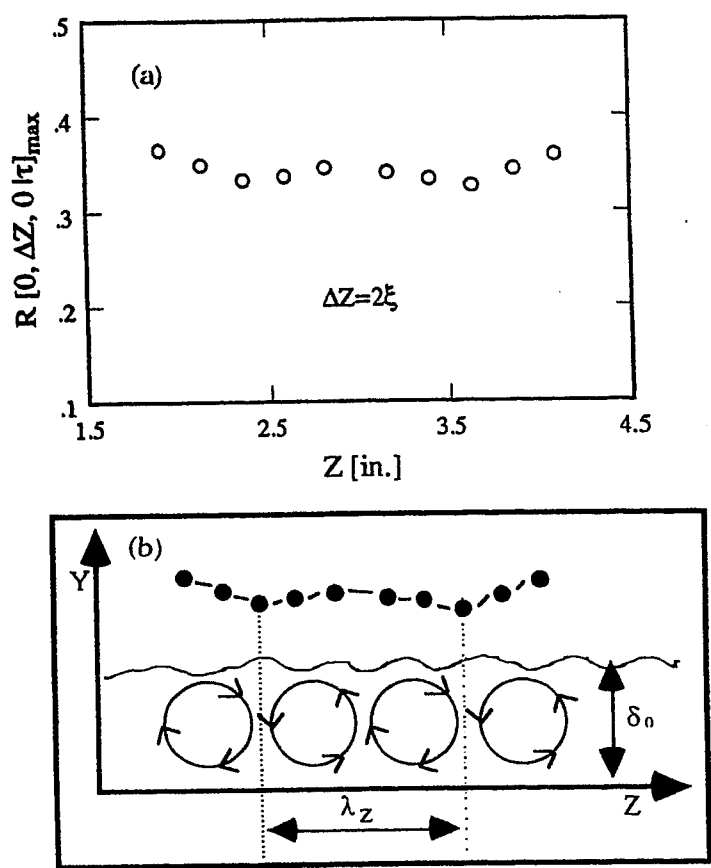


FIGURE 17. a) Variation of maximum cross-correlation coefficient across tunnel floor span; b) hypothetical vortex system.

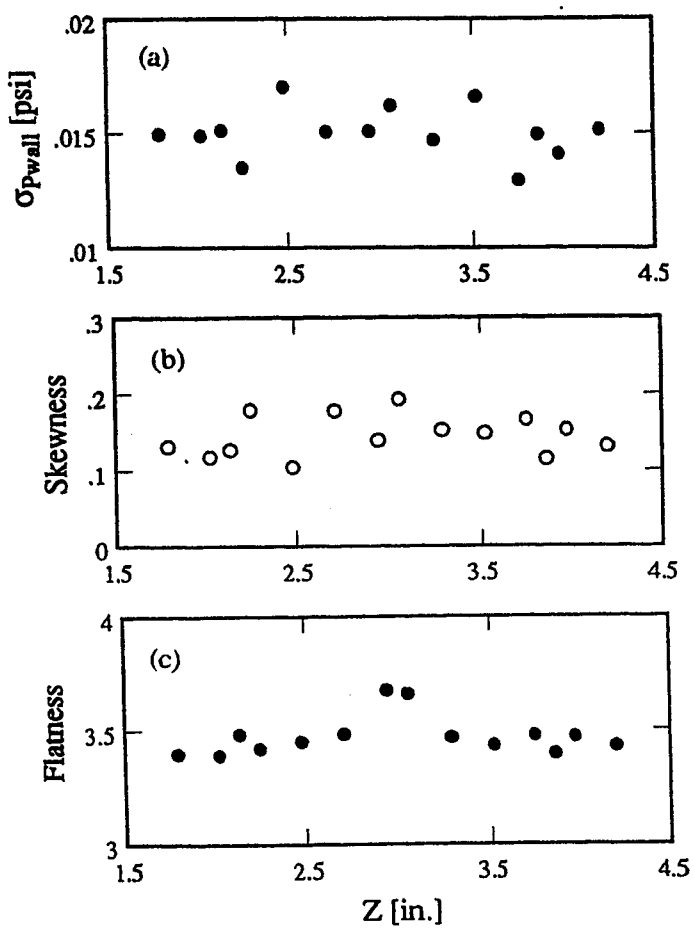


FIGURE 18. Spanwise variation of a) rms wall pressure; b) skewness coefficient; c) flatness coefficient.

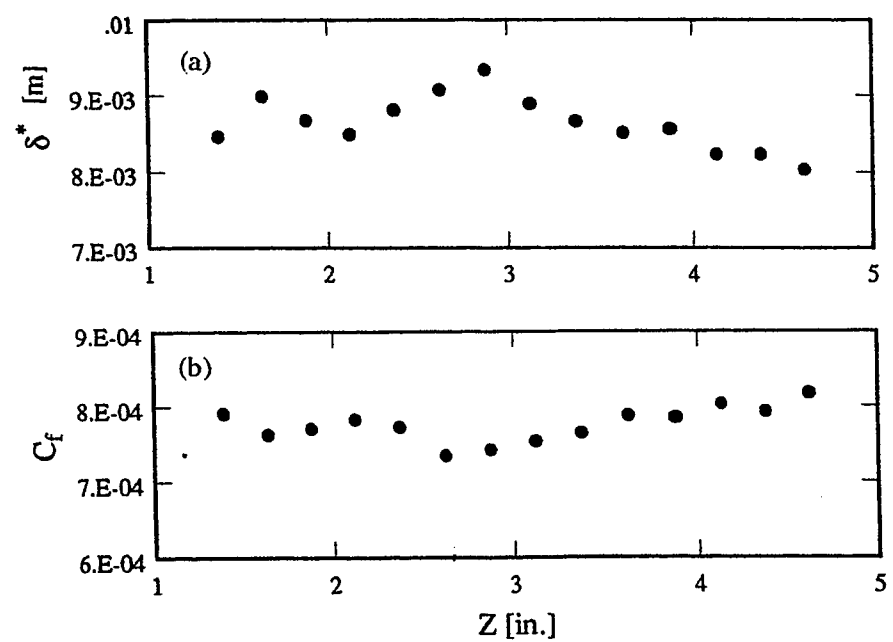


FIGURE 19. Spanwise variation in displacement thickness and in skin friction coefficient.

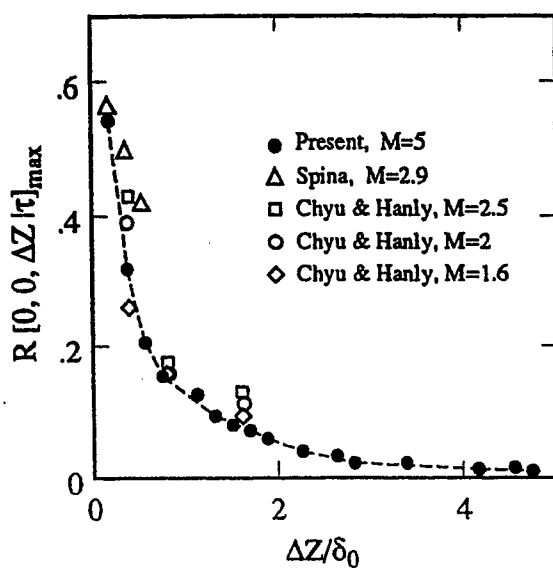


FIGURE 20. Decay of maximum cross-correlation coefficient as a function of  $\Delta z / \delta_0$ .

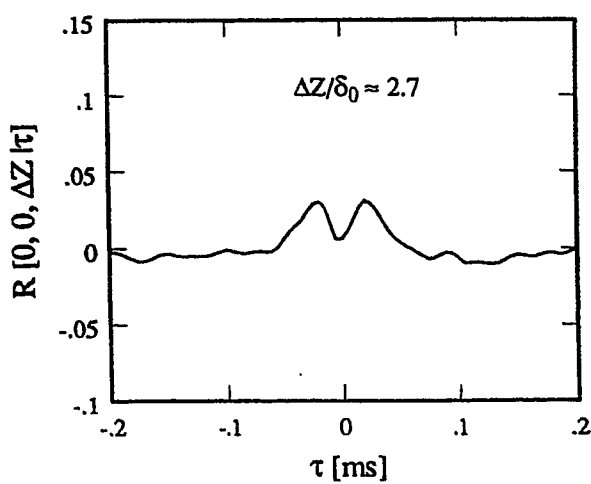


FIGURE 21. Example of spanwise cross correlation with unexpected features.

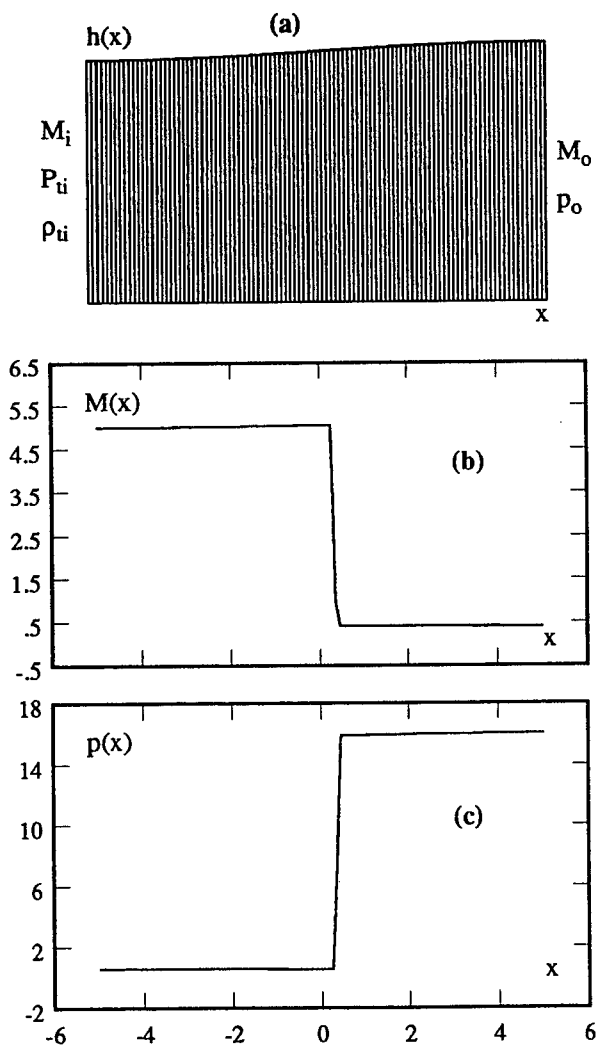


FIGURE 22. Channel geometry, and steady-state solutions for Mach number and pressure.

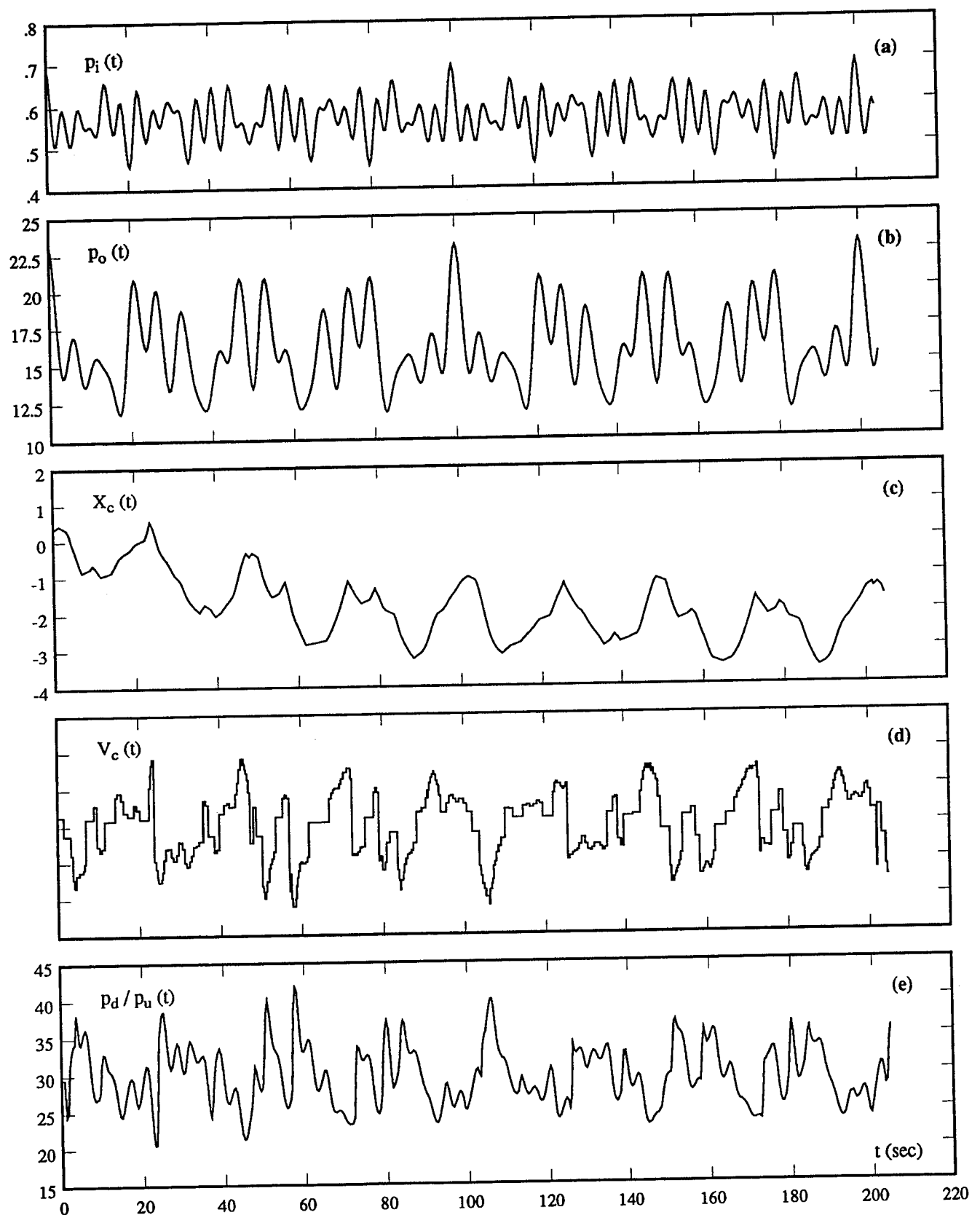


FIGURE 23. Sample histories of inlet,  $p_i(t)$  and outlet,  $p_o(t)$  pressure, and normal shock position,  $X_c(t)$ , velocity,  $V_c(t)$ , and pressure ratio,  $R_c(t)$ .

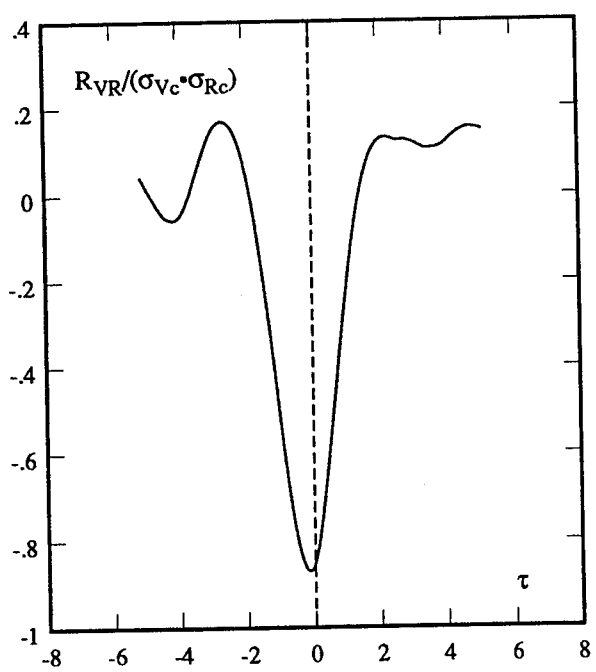


FIGURE 24. Normalized cross-correlation of normal shock

velocity,  $V_c(t)$  and pressure ratio,  $R_c(t)$ .